batteries

MDPI

Article

Impact Response of a Thermoplastic Battery Housing for Transport Applications

Aikaterini Fragiadaki and Konstantinos Tserpes *

Laboratory of Technology & Strength of Materials, Department of Mechanical Engineering & Aeronautics, University of Patras, 26500 Patras, Greece; a.fragkiadaki@ac.upatras.gr
* Correspondence: kitserpes@upatras.gr

Abstract

The transition to electric mobility has intensified efforts to develop battery technologies that are not only high-performing but also environmentally sustainable. A critical element in battery system design is the structural housing, which must provide effective impact protection to ensure passenger safety and prevent catastrophic failures. This study examines the impact response of an innovative sheet molding compound (SMC) composite battery housing, manufactured from an Elium resin modified with Martinal ATH matrix, reinforced with glass fibers, that combines fire resistance and recyclability, unlike conventional thermoset and metallic housings. The material was characterized through standardized mechanical tests, and its impact performance was evaluated via drop-weight experiments on plates and a full-scale housing. The impact tests were conducted at varying energy levels to induce barely visible impact damage (BVID) and visible impact damage (VID). A finite element model was developed in LS-DYNA using the experimentally derived material properties and was validated against the impact tests. Parametric simulations of ground and pole collisions revealed the critical velocity thresholds at which housing deformation begins to affect the first battery cells, while lower-energy impacts were absorbed without compromising the pack. The study provides one of the first combined experimental and numerical assessments of Elium SMC in battery enclosures, emphasizing its potential as a sustainable alternative for next-generation battery systems for transport applications.

Keywords: thermoplastic; SMC; battery; housing; impact; drop tower; LS Dyna; safety

check for updates

Academic Editor: Pascal Venet

Received: 10 September 2025
Revised: 26 September 2025
Accepted: 3 October 2025
Published: 5 October 2025

Citation: Fragiadaki, A.; Tserpes, K. Impact Response of a Thermoplastic Battery Housing for Transport Applications. *Batteries* **2025**, *11*, 369. https://doi.org/10.3390/batteries11100369

Copyright: © 2025 by the authors. Licensee MDPI, Basel, Switzerland. This article is an open access article distributed under the terms and conditions of the Creative Commons Attribution (CC BY) license (https://creativecommons.org/licenses/by/4.0/).

1. Introduction

Driven by the need for a more sustainable transportation sector, aiming to reduce greenhouse gas emissions and dependency on fossil fuels, Battery Electric Vehicles (BEVs) have gained major recognition in recent decades. Their core component, the battery, is the subject of intensive research and development. The most common battery type in contemporary electric vehicles is lithium-ion, which is adopted due to its high energy density [1]. While improvements in battery capacity and charging speed are crucial for extending range in transportation to match conventional vehicles, they often lead to an increase in battery, and consequently, vehicle weight. Current BEVs are heavier than their internal combustion engine counterparts, therefore opting for lightweight materials in the design of the vehicle remains crucial [2]. Composite materials and, more specifically, composite battery housings offer an excellent solution, providing superior weight-specific mechanical performance and enhanced corrosion resistance and thermal insulation compared to traditional aluminum alloy or steel housings [3].

Thermoset matrices have been the state-of-the-art choice compared to their thermoplastic counterparts, due to their easier fiber impregnation, lower processing temperatures, and lower cost [4]. However, thermoplastic resins present greater fatigue resistance, superior damage tolerance under impact, and shorter processing times. Also, thermosets undergo irreversible chemical formation during curing, which permanently sets their molecular structure, while thermoplastics can be remolded while fully retaining their original composition and properties, offering significant benefits for recyclability [5]. Essentially, there is a need for a thermoplastic resin that exhibits good mechanical properties and room-temperature curing but is also compatible with liquid processing techniques. These requirements led to the development of a new acrylic resin by Arkema company, called Elium. This low-viscosity, in situ polymerizable thermoplastic resin effectively cures at room temperature and is suited for both Vacuum-Assisted Resin Infusion (VARI), Resin Transfer Molding (RTM), as well as SMC processes [6,7].

The composite housing design needs to include reliable protection for internal electronics and battery cells. This requires shielding from external loads, e.g., physical impacts, and various environmental influences, such as extreme temperatures, which can cause thermal runaway, the catastrophic overheating of the battery that can lead to fire [8,9]. Consequently, the impact safety of battery pack systems (BPSs) is of great importance [10,11]. Impact events, such as those from road debris, can cause nonvisible internal damage to conventional unidirectional (UD) composites, which reduces their mechanical performance. Discontinuous fiber composites, such as SMCs, appear to be a suitable substitute, providing improved resin flow and complex geometry manufacturing of components at a reduced cost [12]. Within the existing literature, numerous impact studies have been conducted on continuous carbon and glass fiber composites. Carbon fibers are recognized for their high strength, whereas glass fibers exhibit greater ductility, which allows glass fibers to enhance energy absorption before failure, consequently improving the overall impact tolerance of the composite [13]. However, a significant gap exists in comprehensive experimental data, and numerical simulations are needed to thoroughly evaluate the impact resistance of Battery Pack Structures (BPSs) [14,15]. Research on BPS safety predominantly concentrates on cells and the module's electrochemical degradation. Regarding their mechanical integrity, limited impact scenarios including frontal, side, and rear impacts have been examined [16]. Chen et al. investigated the dynamic response of lithium-ion battery packs under high-speed impact, developing models to predict internal failure mechanisms under mechanical abuse [17,18]. Xu et al. examined the influence of State of Charge (SOC) on the mechanical response of lithium-ion batteries during impact [19]. More recently, bottom crashworthiness has gained attention, with researchers utilizing composite materials and structures to enhance impact resistance [10]. Xia et al. introduced a new analysis method designed to evaluate potential damage of battery packs from road debris [20]. Also, explicit finite element analysis (FEA), using the LS-DYNA software, has been employed to model the response of cylindrical lithium-ion battery cells to lateral impact [11] and to simulate the ground impact of lithium-ion battery packs in electric vehicles [21–23].

Concerning the dynamic response of battery enclosures, numerical simulations to predict the deformation of steel battery housings during frontal low-speed impacts have been employed using LS-DYNA software [16]. Ground impact simulations have been developed for fiber metal laminate (FML) battery enclosures, investigating various impact velocities (35–41 m/s), with experimental tests carried out to validate these models [24]. A crash simulation analysis focusing on a battery pack that integrates cylindrical cells within an ABS enclosure has also been carried out using the Radioss solver, aiming to compare the impact responses of the battery pack system both in the presence and absence of shock absorbers [25]. Also, side pole impact simulations on carbon fiber-reinforced

battery enclosures, have been carried out, modeled with VPS software and 2D shell elements [3,10]. Another study examined the design optimization of a battery pack enclosure (BPE) constructed from steel, aluminum, and carbon fiber composite to enhance its impact resistance. This research used a multi-objective optimization approach, integrating numerical models and analytical methods, to reduce BPE's mass and maximum deformation. For this, a modified TOPSIS method was applied to determine the most important design parameters [26].

To the authors' knowledge, a limited number of studies, both numerical and experimental, focusing on the impact performance of SMCs and discontinuous fiber composites have been conducted and no prior work on the impact response of Elium glass fiber SMC battery housings has been reported. In this work, a novel thermoplastic battery enclosure is subjected to ground and frontal pole impact, with parametrically increasing the impact velocity. In Section 2, the SMC material is characterized in tension, compression, shear and three-point bending, and its mechanical properties are calculated. Also, the experimental procedure of drop tower impact tests is described, for both thermoplastic plates and the battery housing, conducted at impact energies of 7.5 J and 30 J. Section 3 outlines the numerical modeling in detail. This includes the development of two models intended to validate the drop tower test results for both the SMC plate and the housing, as well as the development of the parametric ground and crash impact simulations. Section 4 includes the results of numerical modeling that validate the impact response of the housing. Using the validated model, the results of the parametric analysis, for ground and pole impact, are discussed. In Section 5, the work of this paper is summarized.

2. Experimental

2.1. Geometry and Material

The battery housing consists of two primary components, the lid and the main enclosure, both fabricated from a novel thermoplastic composite material. The matrix is based on Arkema Elium MC 590, an acrylic resin, modified with Martinal ATH (aluminum hydroxide) to impart fire resistance. The composite is reinforced with 20 wt% chopped glass fibers (JM Multistar 272), providing mechanical strength and stiffness. The housing has maximum external dimensions of 440 mm × 300 mm × 89 mm and features four symmetrical support legs at the bottom, each measuring 12 mm × 12 mm × 2 mm (width × length × height), as illustrated in the CAD drawing of Figure 1. Due to the manufacturing process, the wall thickness of the housing varies between 3.0 and 3.5 mm. The material is produced in the form of a Sheet Molding Compound (SMC), which is a specialized type of prepreg suitable for compression molding. The complete manufacturing process, from the formulation of semi-finished SMC sheets to the compression molding of flat plates and the final housing component, was carried out at Fraunhofer ICT in Pfinztal, Germany [2].

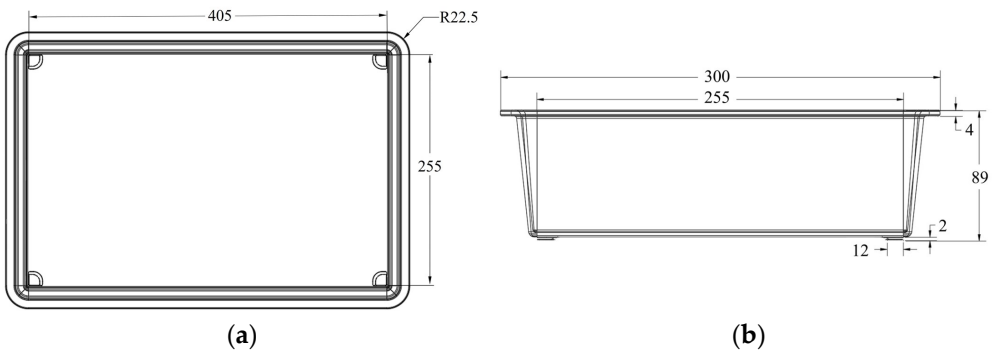

Figure 1. Geometry and dimensions (in mm) of the housing: (**a**) x-y plane; (**b**) y-z plane.

2.2. Mechanical Characterization of the SMC Composite

To characterize the short fiber SMC composite, tension, compression, shear and three-point bending tests were conducted in accordance with relevant ASTM standard test methods. For each mechanical test, a minimum of five specimens were prepared and tested under controlled environmental conditions of 23 °C and 50% relative humidity, in compliance with the respective standard procedures. Strain measurements were obtained using bonded strain gauges with a resistance of 350 Ω. All tests were carried out using a 100 kN MTS Universal Testing Machine equipped with hydraulic grips. Consistent with the nature of the composite—comprising randomly oriented short glass fibers—specimens were tested without end tabs, as permitted by the applicable ASTM standards. The testing configurations and the mounted specimens are shown in Figure 2. A summary of the testing procedures and associated parameters is provided in Table 1.

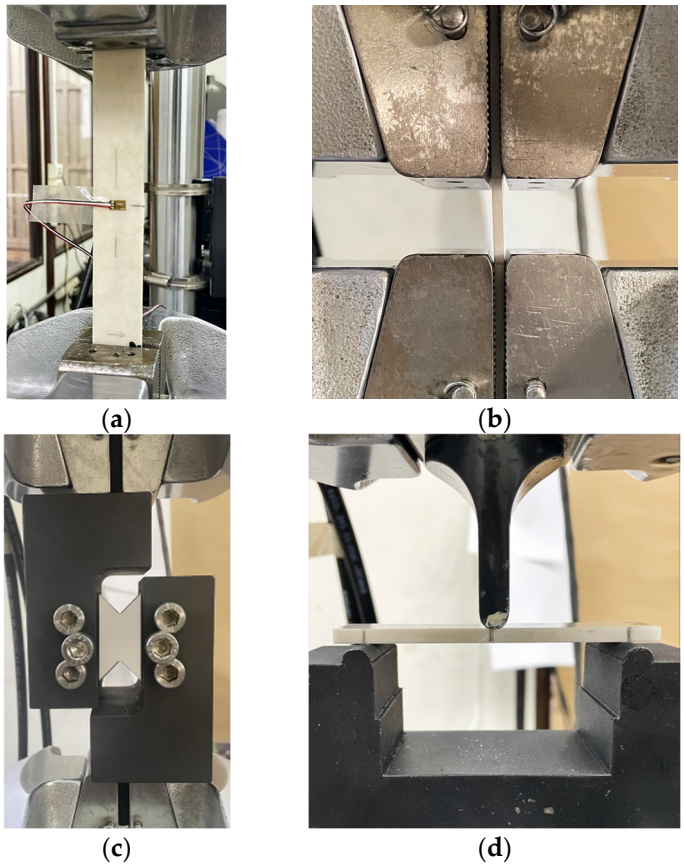

Figure 2. Testing configuration and mounted specimens of (**a**) tension test, (**b**) compression test, (**c**) shear test, and (**d**) three-point bending test.

Table 1. Mechanical testing parameters.

Test	Standard	Specimen Dimensions	Speed of Testing
Tension	ASTM D3039	250 × 25 × 2.5 mm^3	1 mm/min
Compression	ASTM D3410	140 × 25 × 2.5 mm^3	1 mm/min
Three-point bending	ASTM D790	95 × 18 × 4.5 mm^3	2.2 mm/min
Shear	ASTM D7078	76 × 56 × 4.5 mm^3	2 mm/min

Tensile properties of the composite material were evaluated in accordance with ASTM D3039. Flat strip specimens with a constant rectangular cross-section were used, measuring 250 mm × 25 mm × 2.5 mm, with a gage length of 150 mm. The specimens were mounted in the universal testing machine and subjected to tensile loading at a standard crosshead

displacement rate of 1 mm/min. Strain gauges with a resistance of 350 Ω were affixed on both faces of the specimen, one aligned in the longitudinal direction and the other in the transverse direction. These measurements enabled the calculation of the tensile modulus of elasticity and Poisson's ratio, based on the stress–strain data and using equations specified in ASTM D3039. Additionally, the ultimate tensile strength (UTS) of the material was determined as part of the test output.

Compression testing was conducted in accordance with ASTM D3410. Rectangular flat specimens were prepared with dimensions of 140 mm (length) × 25 mm (width) × 2.5 mm (thickness) and a gage length of 12 mm. The gage length was determined based on the specimen thickness to ensure sufficient space for the placement of strain gauges in the longitudinal direction, while also minimizing the risk of Euler buckling within the test section. Specimens were mounted in the testing machine and compressed at a constant crosshead displacement rate of 1 mm/min. The test yielded measurements of ultimate compressive strength and compressive modulus.

Flexural testing was carried out according to ASTM D790, using a three-point bending configuration. Specimens had a rectangular cross-section with dimensions of 95 mm × 18 mm × 4.5 mm and were tested using a support span-to-depth ratio of (16 ± 1):1, as recommended by the standard. The crosshead speed was set to 2.2 mm/min. This procedure enabled the evaluation of key flexural properties, specifically the flexural strength and flexural modulus.

Shear properties were evaluated in accordance with ASTM D7078, which utilizes v-notched rail shear specimens. In this method, the specimens are clamped between two loading fixtures and subjected to tensile loading, which induces a relatively uniform shear stress distribution in the reduced cross-section of the gage area, ultimately resulting in shear failure. To measure shear strain, two strain gauges are applied at ±45° angles relative to the loading direction. The test was performed at a crosshead speed of 2 mm/min. The test results were used to determine the shear modulus and ultimate shear strength of the composite material.

Experimental Results

Figure 3 presents the force–displacement curves obtained from the mechanical testing procedures, while Table 2 summarizes the corresponding mechanical properties derived from each test. The experimental results demonstrate that the short fiber SMC composite exhibits a transversely isotropic mechanical response, characterized by comparable properties in both the in-plane and through-thickness directions. This behavior is consistent with the random orientation of the chopped glass fibers within the matrix, contributing to a relatively uniform distribution of mechanical performance across different loading directions. The failure modes of the specimens are illustrated in Figure 4.

Table 2. Mechanical properties of the SMC composite derived from standardized testing.

Property	Value
Modulus of Elasticity	12.26 GPa
Tensile strength	94.99 MPa
Poisson's ratio	0.15 (-)
Compressive modulus	13.61 GPa
Compressive strength	133.83 MPa
Flexural modulus	12.91 GPa
Flexural strength	190.31 MPa
Shear modulus	5.8 GPa
Shear strength	76.92 MPa

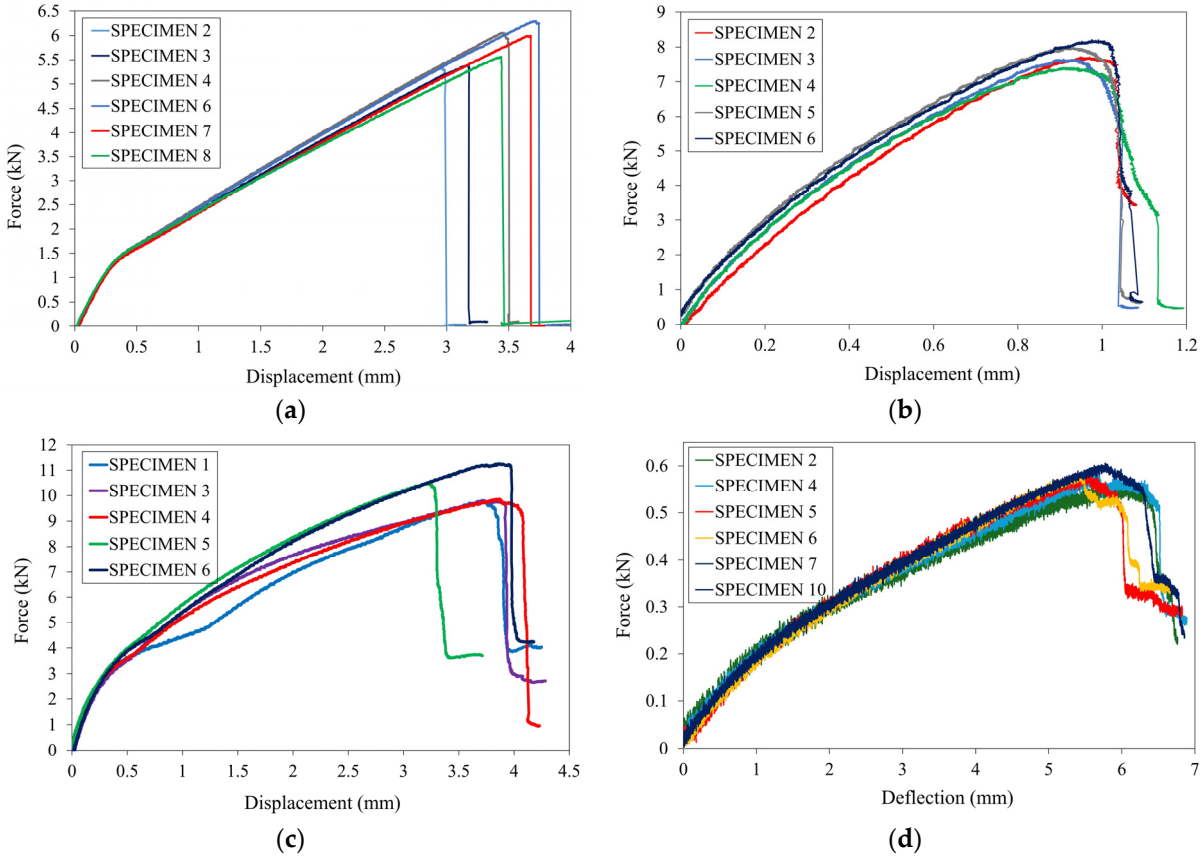

Figure 3. Force-displacement curves of the SMC specimens subjected to (**a**) tension, (**b**) compression, (**c**) shear, (**d**) three-point bending.

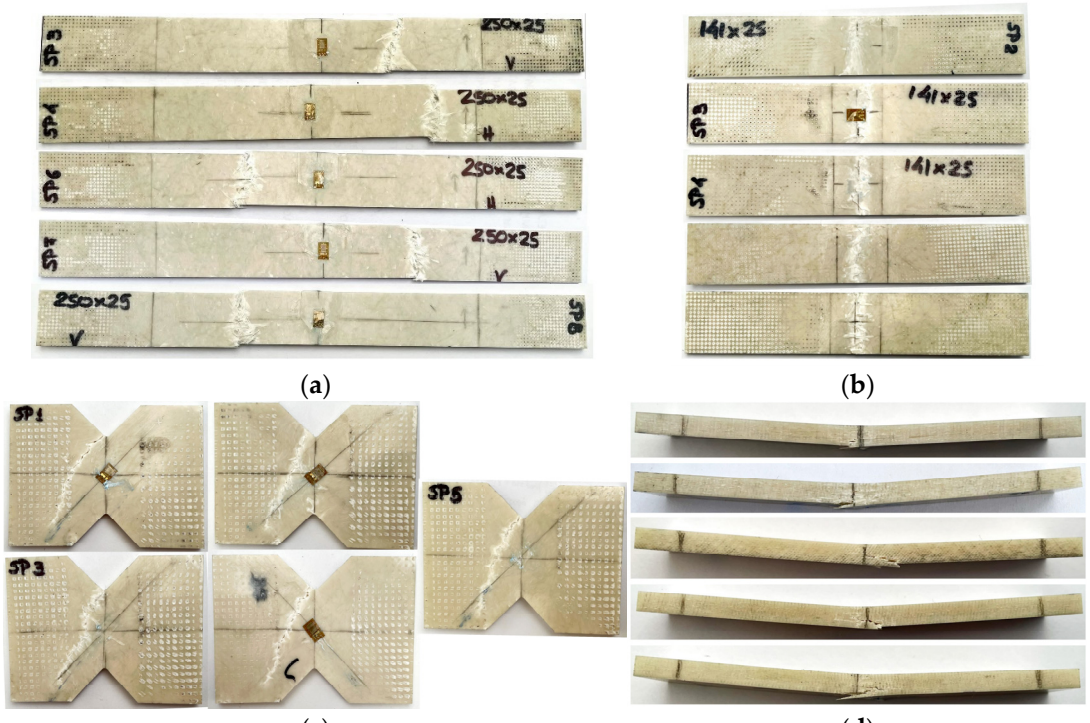

Figure 4. Failure modes of the SMC specimens subjected to (**a**) tension, (**b**) compression, (**c**) shear, (**d**) three-point bending.

The tensile behavior of the composite material exhibits a bi-linear force–displacement response, as illustrated in a. The initial linear segment of the curve corresponds to the elastic region, primarily governed by the presence of a high concentration of aluminum hydroxide ($Al(OH)_3$) within the thermoplastic matrix. The $Al(OH)_3$ filler acts as a stress concentrator, restricting the mobility and alignment of the polymer chains under tensile loading. This interaction results in a stiffening effect, which enhances the initial stiffness and elastic modulus of the composite. However, this same mechanism contributes to a reduction in ductility, as the restricted polymer chain mobility limits the material's ability to undergo plastic deformation. Consequently, the composite exhibits a more brittle response in the post-elastic region, consistent with the reduced strain-to-failure observed in the experimental data [27]. However, with the increase in the filler content, the continuity of the polymer matrix decreases, resulting more in $Al(OH)_3$ particle-particle interaction rather than particle–resin interaction [28]. The formation of particle clusters, also, increases porosity and has a degrading effect on interface adhesion, which accelerates crack propagation and can lead to poor mechanical attributes [29]. The linear region, following the initial one, shows a drastic drop of the incline of the curve, thus a smaller tangent modulus (3.68 GPa) compared to the elastic modulus (12.26 GPa). This can be attributed to the thermoplastic resin, which gradually becomes less effective as the reinforcements begin to dominate the material's response [30]. The softening in the mechanical response is also developed due to matrix cracking and poor filler–resin interface bonding. The linear behavior is maintained until the material reaches a brittle failure. As illustrated in Figure 4a, the failure mechanisms due to tension exhibit matrix cracking, fiber breakage and fiber pullout.

Under compressive loading, fiber breakage is not the primary failure mode [6]. Instead, the material tends to undergo degradation due to crack initiation and propagation, as well as debonding between the fibers and matrix. Due to the thermoplastic behavior of the Elium resin, that has a low yield point [7], the initial elastic region, shown in Figure 4b, is not easily noticeable, because of the early development of microcracks resulting in non-linearity. Following the crack propagation, the ultimate compressive strength of the SMC is achieved, and a sudden drop of the load is observed, leading to the ultimate fracture of the composite. Figure 4b displays the specimens after fracture, highlighting matrix cracking and fiber debonding as the main failure mechanisms.

Concerning the shear response of the composite material, as illustrated in Figure 4c, the initial behavior is linear elastic, enabling the determination of the shear modulus. As strain increases, the material exhibits a non-linear response, attributed to the initiation and growth of micro-cracks within the thermoplastic resin matrix, a characteristic behavior of Elium-based composites. At higher deformation levels, a visible diagonal crack forms at the notch root, as shown in Figure 4c, leading to a slight reduction in the load response just prior to ultimate failure.

Regarding the three-point bending results, the composite exhibits high flexural strength, indicating effective interfacial bonding between the matrix and the reinforcing fibers [6]. In terms of flexural failure modes, Figure 4d shows that crack initiation consistently occurs on the tension side of the specimen, with fracture localized at the mid-span, corresponding to the region of maximum bending stress.

2.3. Drop Tower Impact Tests

Low-velocity impact tests were conducted using an INSTRON 9250HV drop tower machine, as shown in Figure 5. A 45 kN load cell was employed to accurately record the force exerted by the impactor during each test. The system is equipped with an anti-rebound mechanism to prevent multiple impacts on the specimen, ensuring consistency in

test results. All tests were performed using a steel impactor with a mass of 6.795 kg, while the impact energy was controlled by adjusting the drop height, following the principle of energy conservation. The impactor was fitted with a 16 mm diameter hemispherical tip, in compliance with ASTM D7136 guidelines, to ensure standardized testing conditions. The impactor was mounted on a crosshead, which lifted it to the predetermined height before releasing it for free-fall along two vertical guide columns.

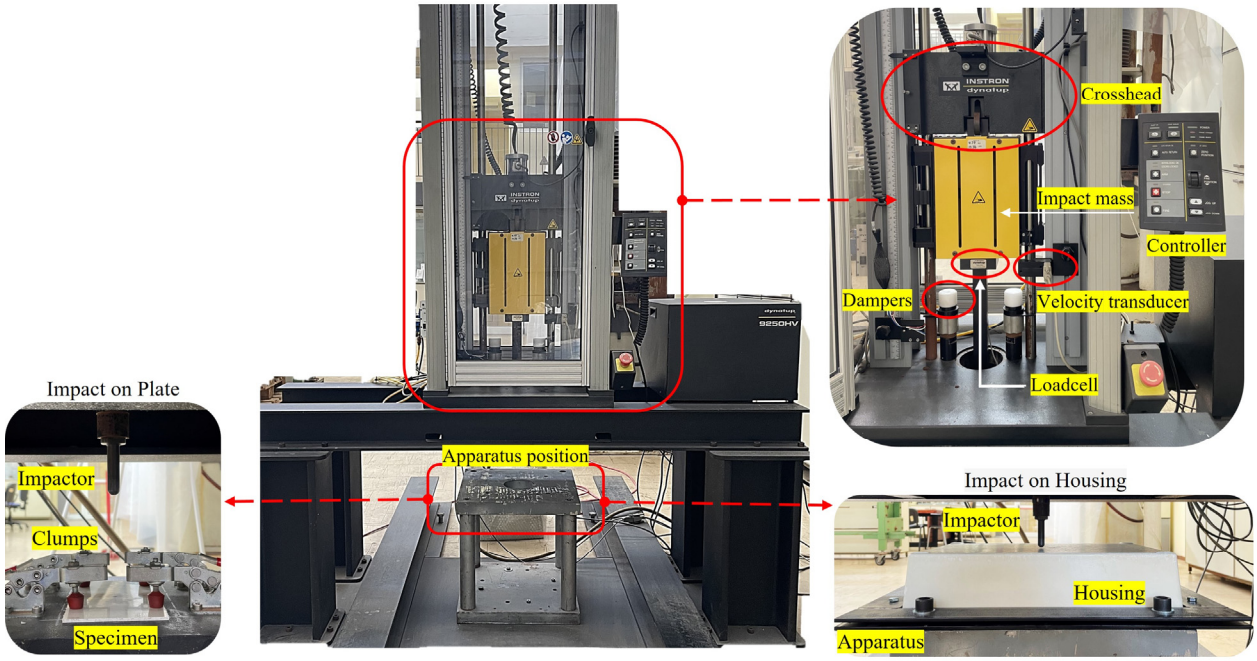

Figure 5. Instron drop tower testing setup.

The data acquisition system records the load vs. time response for each impact event. The impact velocity is measured immediately prior to contact using a photoelectric diode and flag system. This system employs a flag attached to the drop weight, consisting of two prongs spaced 1 cm apart. As the prongs pass through the photo-diode sensor, the obstruction of the light beam generates electrical signals. The system calculates the time interval between the leading edges of the two prongs as they interrupt the beam. Given the known distance between prongs (1 cm) and the measured time, the impact velocity of the drop weight is accurately determined using basic kinematic principles. This method ensures precise velocity measurement at the moment just before impact.

Impact tests were performed at two energy levels, 7.5 J and 30 J, corresponding to impact velocities of 1.486 m/s and 2.972 m/s, respectively. Two SMC plate specimens were tested at each energy level. The plates were cut to dimensions of 165 mm × 100 mm × 2.5 mm and positioned on a 250 mm × 250 mm × 30 mm steel support base featuring a 130 mm × 70 mm central opening. The specimens were secured using four symmetrical clamps to ensure proper fixation during impact. For the battery housing, testing was conducted at an impact energy of 30 J. A custom fixture was designed to maintain the housing in a fixed position throughout the test. A steel plate measuring 540 mm × 400 mm was placed beneath the housing to provide structural support, while a second steel plate of the same dimensions, containing a 450 mm × 280 mm cut-out, was positioned on top. The two plates were clamped together using eight bolts, each with an 18 mm diameter, ensuring a rigid and repeatable setup. Following each test, the damage depth was measured at the center of the specimen, where the most significant deformation or damage consistently occurred.

3. Numerical Modeling

In this study, all geometries were designed and meshed using Ansys 2025 R1Workbench, while the impact simulations were carried out using the LS-DYNA explicit solver. Explicit time integration is particularly well suited for problems involving significant non-linearities, such as complex contact interactions and non-linear material behavior, which are common in impact scenarios. However, explicit methods require a small time step to maintain numerical stability and ensure accurate results. The time step size is governed by the transit time of an acoustic wave through the smallest element in the model, as defined by the shortest characteristic length. This is a function of the material's elastic properties—specifically, the Young's modulus, Poisson's ratio, density, and speed of sound [31]. According to the Courant condition, information should not propagate through more than one element per time step; otherwise, numerical instabilities may arise, leading to spurious oscillations and non-physical results. To enhance stability, the Time Step Scale Factor (TSSFAC), typically set at 0.90, was conservatively reduced to 0.70 in this study. This ensures a safer margin for accurate and stable calculations. For the structural discretization, solid elements were used with ELFORM = 1, a reduced integration formulation featuring a single integration point. While computationally efficient, this formulation is susceptible to hourglass modes, which require stabilization. To address this, stiffness-based hourglass control (Type 4) was employed. This control method is particularly effective in impact simulations involving structural components, especially when used with a reduced hourglass coefficient of 0.05, which minimizes the introduction of artificial stiffness and preserves the physical fidelity of the simulation.

3.1. Drop Tower Impact Models

The development of the drop tower numerical models stems from the need to validate the simulated impact response against experimental data, ensuring that the model reliably captures the physical behavior of the system. Model validation is essential for establishing the credibility and accuracy of the simulation framework. Once validated, the model serves as a powerful tool to significantly reduce testing costs and time, while enabling the prediction of structural performance under conditions that may be difficult, expensive, or unsafe to replicate experimentally. The validated model will be utilized in Sections 3.2 and 3.3 to support the numerical analysis of parametric ground and crash impact scenarios, respectively, providing predictive insights into the mechanical performance and crashworthiness of the battery housing system.

3.1.1. Model of SMC Plate

The first drop tower model simulates the impact event of a projectile striking the SMC composite plates. The setup replicates the configuration of the experimental drop tower apparatus, including the steel support base with a central orthogonal opening, the four clamps, and the steel impactor, as illustrated in Figure 6. These three components are modeled as rigid bodies using Material Model 20 (MAT_RIGID) in LS-DYNA, with the associated material parameters listed in Table 3. The MAT_RIGID formulation enables the definition of both translational and rotational constraints for each component. Specifically, the base and clamps are fully constrained in all degrees of freedom, while the impactor is restricted only in the x and y directions and all rotational degrees of freedom, allowing free motion solely in the z-translational direction to simulate the vertical drop impact accurately.

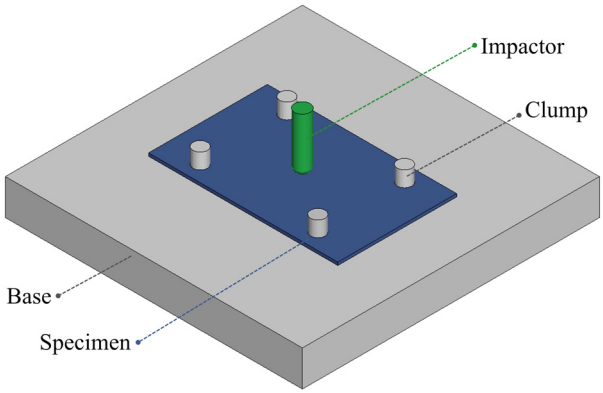

Figure 6. Configuration of the drop tower model for the plate.

Table 3. Steel input parameters for MAT_20.

Parameter	Value
Density, RO	7580 kg/m^3
Young's modulus, E	200 GPa
Poisson's ratio, PR	0.33 (-)

A refined mesh was employed to ensure numerical stability and capture local effects with high accuracy. Specifically, 1 mm solid elements were used for the impactor and the clamps, while a 2 mm element size was applied to the composite plate, as shown in Figure 7a,b,d. This mesh resolution was selected to minimize the influence of non-linearities that could introduce numerical instabilities during the simulation. The specimen, representing the SMC composite plate, was modeled using Material Model 162 (MAT_COMPOSITE_MSC_DMG) in LS-DYNA. This material model enables progressive failure analysis of composite materials, incorporating the Hashin failure criteria and a damage mechanics-based softening behavior following damage initiation [32]. Given the randomly oriented chopped glass fibers in the SMC, the composite exhibits transversely isotropic behavior, with identical in-plane properties and reduced out-of-plane strength. This behavior effectively mimics a unidirectional (UD)-like response, which is implemented in the model using option 1 of the AMODEL keyword, that assumes transverse isotropy. The material properties were derived from experimental mechanical tests presented in Section 2, and the full list of input parameters is provided in Table 4. However, polymer-based composites are strain-rate sensitive, indicating different failure modes under quasi-static and dynamic loadings [33,34]. It should be acknowledged that in this study, no high-strain-rate characterization has been carried out. With that said, MAT_162 has the ability to implement the effects of the strain-rate-dependent non-linear stress–strain response of the composite via the CERATE parameters, which is modeled by a logarithmic strain-rate-dependent function for the moduli and strength in the form of

$$\frac{X_{RT}}{X_0} = 1 + C_{rate} ln\left(\frac{\dot{\bar{\varepsilon}}}{\dot{\bar{\varepsilon}_0}}\right), \quad (1)$$

where X_{RT} is the rate-dependent property of interest at an average strain rate of $\dot{\bar{\varepsilon}}$, X_0 is the quasi-static property of interest at an average reference strain rate of $\dot{\bar{\varepsilon}_0}$ (1/s). CERATE1 is used to add rate effects on strength properties, whereas CERATE2, CERATE3 and CERATE4 are used to add rate effects on three axial and three shear moduli. More specifically, CERATE2 affects the two axial moduli Ea and Eb, CERATE4 controls the through-the-thickness modulus, Ec, and CERATE3 controls the rate effects on the shear moduli, Gab, Gbc and Gca.

It should be noted that the through-the-thickness tensile strength and the shear strengths are not considered strain-rate-dependent in the MAT_162 formulation [35]. The CERATE parameters were selected by literature values for similar polymer composites [35–37], since no dynamic testing was performed for the material, which partially mitigates the limitation and ensures that the simulations reflect dynamic stiffening effects to a reasonable extent. In terms of meshing, the SMC plate was discretized using 1 mm solid elements, as illustrated in Figure 7c.

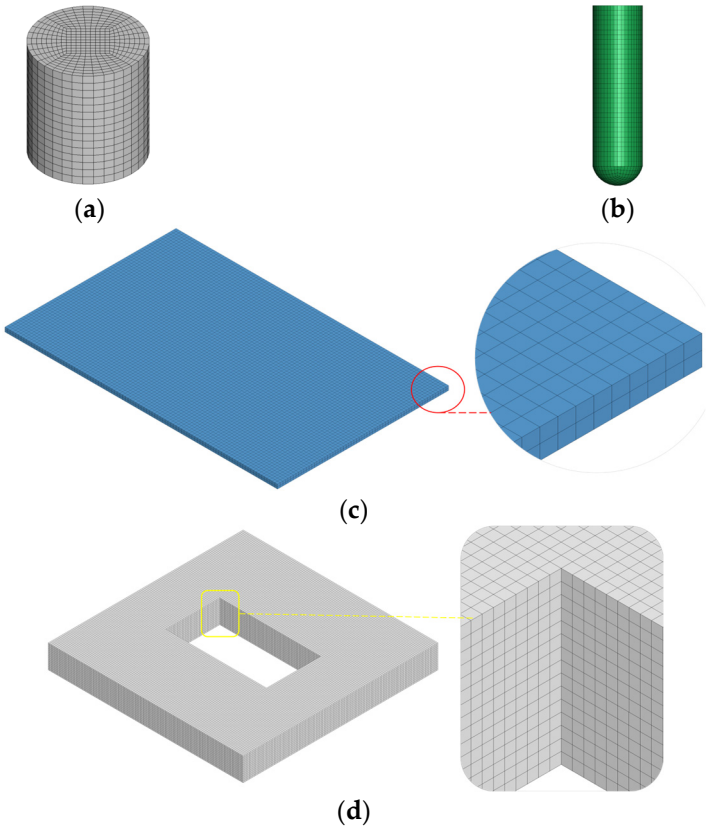

Figure 7. FE mesh of the drop tower model components for the plate: (**a**) clump, (**b**) impactor, (**c**) plate, and (**d**) base.

In impact simulations, automatic contact definitions are preferred due to the continuously changing relative orientations and the large deformations that typically occur during the event. Accordingly, CONTACT_AUTOMATIC_SURFACE_TO_SURFACE was selected in LS-DYNA to define the interactions between the composite specimen and both the steel base plate and the impactor. According to the literature, static friction coefficients for contact between glass fiber-reinforced polymers (GFRPs) and steel typically range from 0.2 to 0.5, while dynamic friction coefficients are generally 30–40% lower [38]. In this study, the static and dynamic friction coefficients for the contact between the GF composite and steel components (impactor and base) were set to 0.4 and 0.2, respectively, to reflect realistic interaction conditions and ensure numerical stability.

To accurately model the interaction between the composite specimen and the clamps, a tied contact approach was implemented. Specifically, CONTACT_TIED_SURFACE_TO_SURFACE_OFFSET was used, which is well-suited for interactions involving rigid bodies, such as the clamps in this setup. In this configuration, the slave nodes (clamps) are constrained to follow the motion of the master surface (specimen), ensuring consistent boundary conditions and preventing relative motion at the interface.

Table 4. SMC input parameters for MAT_162.

Parameter	Value
Density, RO	1878 kg/m^3
Young's modulus—longitudinal direction, Ea	12.2 GPa
Young's modulus—transverse direction, Eb	12.2 GPa
Young's modulus—through-thickness direction, Ec	5 GPa
Poisson's ratio, vba	0.15 (-)
Poisson's ratio, vca, vcb	0.18 (-)
Shear modulus, Gab	5.8 GPa
Shear modulus, Gbc, Gca	3.5 GPa
Longitudinal tensile strength, SaT	95 MPa
Transverse tensile strength, SbT	95 MPa
Through-thickness tensile strength, ScT	75 MPa
Longitudinal compressive strength, SaC	133 MPa
Transverse compressive strength, SbC	133 MPa
Matrix mode shear strength, Sab, Sbc, Sca	76 MPa
Strength properties strain rate coefficient, CERATE1	0.024
Longitudinal moduli strain rate coefficient, CERATE2	0.03
Shear moduli strain rate coefficient, CERATE3	0.03
Transverse moduli strain rate coefficient, CERATE4	0.03

The projectile was assigned an initial impact velocity using the INITIAL_VELOCITY_GENERATION keyword in the z-direction, corresponding to the experimental impact energy levels. For the low-velocity impact simulations, two energy levels were investigated: 7.5 J and 30 J, which correspond to initial velocities of 1486 mm/s and 2972 mm/s, respectively.

3.1.2. Model of SMC Battery Housing

The second drop tower simulation model replicates the impact event of a projectile striking the SMC composite housing. To constrain the housing's movement and suppress rebound during the impact event, two steel plates are implemented: one with a rectangular opening matching the dimensions of the housing (positioned on top), and a solid plate (placed underneath). This setup is designed to secure the specimen while allowing localized deformation at the impact site. The projectile is positioned to strike the center of the housing's upper surface, as shown in Figure 8. All three components—the projectile and the upper and lower plates—are modeled as rigid bodies using LS-DYNA's MAT_RIGID material model, with corresponding parameters listed in Table 3. The steel plates are fully constrained in all degrees of freedom, while the projectile is restricted to translational motion along the *z*-axis. In terms of meshing, the steel plates are discretized with 3 mm elements, while the projectile is refined with 0.5 mm elements, as illustrated in Figure 9a. The housing is modeled using MAT_162, as previously detailed in Section 3.1.1. To mitigate hourglass effects and improve contact stability, a localized mesh refinement is applied to the impact zone. Specifically, a 60 mm × 60 mm central area is meshed with 0.5 mm elements, while the remainder of the housing is meshed with 2 mm elements to optimize computational efficiency, as shown in Figure 9b.

An automatic surface-to-surface contact algorithm was employed to define the interactions between the projectile, steel plates, and the SMC composite housing. This contact type was selected to ensure accurate handling of impact events, sliding, and separation between rigid and deformable bodies. As previously specified, the static and dynamic friction coefficients for the steel–composite interfaces were set to 0.4 and 0.2, respectively, to reflect realistic interaction conditions observed in experimental testing. The projectile was assigned an initial velocity in the z-direction, calibrated to match an impact energy of

30 J. This corresponds to an initial impact velocity of 2972 mm/s, derived from the kinetic energy equation and consistent with experimental conditions.

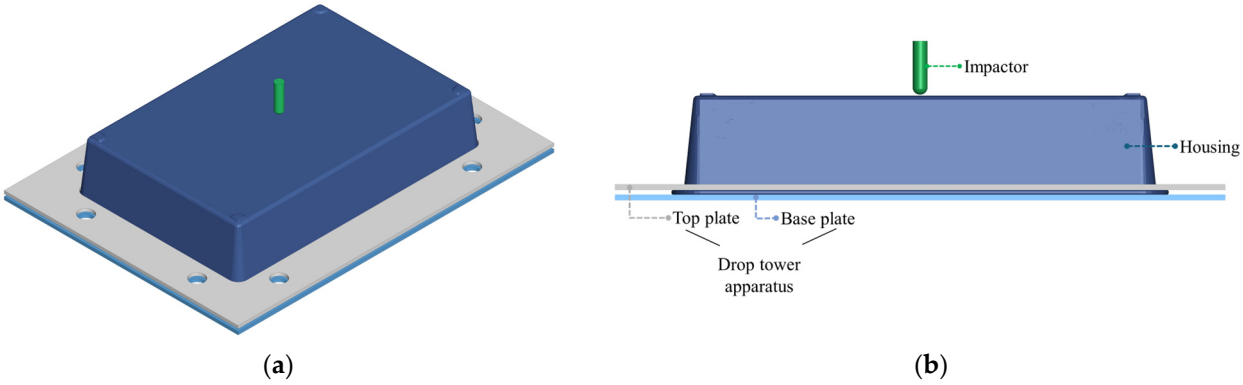

Figure 8. Configuration of the drop tower model for the housing: (**a**) isometric view and (**b**) side view.

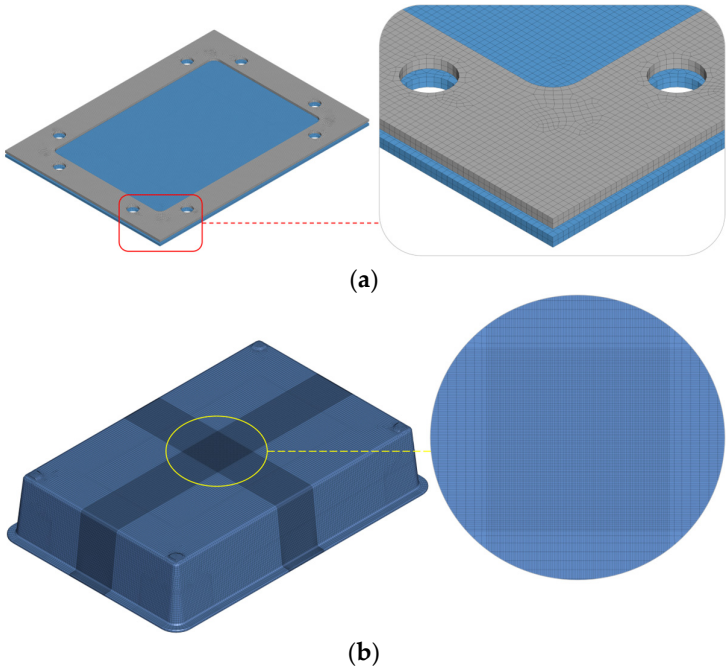

Figure 9. FE mesh of (**a**) the apparatus of the drop tower model for the housing, and (**b**) the housing.

3.2. Ground Impact Model

Investigating ground impact scenarios in battery housing simulations is critical for ensuring the safety and structural integrity of electric vehicles (EVs) under real-world operating conditions. Battery housings play a key role in protecting lithium-ion battery packs, which are highly sensitive due to their high energy density and potential for hazardous failure modes. In typical driving environments, vehicles are routinely subjected to impacts from road debris, curbs, or other low-lying obstacles—especially at high speeds. A severe impact to the underside of the vehicle can inflict mechanical damage on the battery housing, which may propagate to the battery cells, resulting in internal short circuits, electrolyte leakage, or thermal runaway. These failure modes can lead to fires, explosions, and the release of toxic gases, posing a direct threat to both occupant safety and public health. Even when catastrophic failure is avoided, sub-critical impacts can still induce internal damage to the battery structure, leading to performance degradation, reduced driving range, and shortened battery lifespan. Consequently, numerical simulations are indispensable for evaluating the crashworthiness of battery housings, allowing engineers to predict mechani-

cal response, optimize designs, and implement effective countermeasures to prevent both catastrophic and progressive damage.

The FE model developed to simulate ground impact, as shown in Figure 10, includes three main components: the composite battery housing, the lid, and a spherical steel impactor with a diameter of 20 mm and mass of 0.3 kg, representing a road debris impact scenario. The enclosure assembly, comprising the housing and lid, is modeled using the short fiber SMC composite material and is assumed to be adhesively bonded. A hexagonal mapped mesh was generated for all components to ensure mesh quality and accuracy. The battery housing and lid were discretized using 2 mm solid elements, while the impactor was meshed with 1 mm elements to capture detailed contact behavior. The projectile is modeled as a rigid body using MAT_RIGID, constrained to move only in the z-direction to replicate vertical impact. The composite components are defined using MAT_162, as described in Section 3.1.1. To simulate fixed support conditions, the four bottom legs of the battery housing are fully constrained in the z-direction using BOUNDARY_SPC_SET.

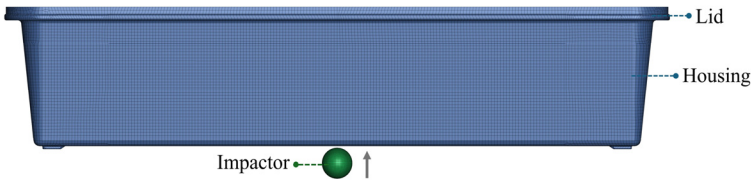

Figure 10. FE mesh of the housing and the impactor of the ground impact model.

An automatic surface-to-surface contact was employed to define the interaction between the impactor and the SMC composite housing, enabling accurate simulation of dynamic contact behavior during impact. Given that the lid and main enclosure are adhesively bonded, a cohesive zone modeling (CZM) approach was adopted to represent the bonded interface. Specifically, the CONTACT_AUTOMATIC_SURFACE_TO_SURFACE_TIEBREAK option was used, which activates only for nodes initially in contact. In this study, Tiebreak Option 9 was selected, which is based on the cohesive material model MAT_138 (MAT_COHESIVE_MIXED_MODE). This option implements a bilinear traction–separation law and a quadratic mixed-mode delamination criterion, along with a progressive damage formulation to simulate interfacial failure mechanisms [31,32]. In CZM, traction stresses develop as bonded nodes begin to separate. Once the predefined maximum traction strength is reached, interfacial failure occurs. This approach effectively captures debonding behavior while maintaining computational efficiency. As demonstrated in the research of Dogan et al. [39], the tiebreak contact model, with appropriately chosen parameters, has shown strong correlation with experimental results and offers a computationally efficient alternative to full CZM implementation. Accordingly, this method was chosen for the current study to balance accuracy and simulation performance. The tiebreak failure parameters used here are representative of typical structural adhesive films and are summarized in Table 5.

Table 5. Delamination damage model input data for Tiebreak contact.

Parameter	Value
Normal failure stress (peak traction), NFLS	40 MPa
Shear failure stress (peak traction), SFLS	60 MPa
Exponent of the mixed mode criterion (Power law), PARAM	2
Normal energy release rate, ERATEN	1.7 MPa·mm
Shear energy release rate, ERATES	0.789 MPa·mm
Tangential stiffness to normal stiffness, CT2CN	1
Normal stiffness, CN	10^6 MPa/mm

Four cases of impact are examined, with a parametric increase in velocity between 10 and 25 m/s, as described in Table 6, which corresponds to a wide range of realistic speeds, 36 to 90 km/h, a vehicle can travel with.

Table 6. Ground impact parameters.

	Impactor's Initial Velocity	Total Energy
i.	10 m/s	15 J
ii.	15 m/s	33.75 J
iii.	20 m/s	60 J
iv.	25 m/s	93.75 J

Model of Cells and Cell Pack

The primary objective of battery housing design is to ensure the protection of individual cells, which significantly influences the overall stiffness, mass, and energy absorption capacity of the battery pack. During an impact event, the housing serves as the first line of defense, transmitting forces directly to the cell pack. Therefore, accurately modeling the cell pack is essential to realistically predict load distribution, deformation behavior, and energy dissipation throughout the system. This level of fidelity is critical for achieving compliance with safety standards and regulations. Omitting the cell pack from the simulation would likely result in an overestimation of the housing's protective capabilities, leading to a misleading evaluation of the battery system's crashworthiness. As such, the inclusion of the cell pack in the numerical model is vital for assessing the structural integrity of the entire assembly and for ensuring the reliable protection of its most critical components under impact conditions.

In this study, a thermoplastic cell pack is placed inside the composite housing, with outer dimensions of 230 mm × 288 mm × 81 mm, as illustrated in Figure 11a. The pack encapsulates five solid-state pouch cells, each measuring 280 mm in length and 195 mm in width, utilizing aluminum–plastic enclosures and Li/Advanced LFP (Lithium Iron Phosphate) battery chemistry. As the focus of this study lies in evaluating the mechanical response rather than the electrochemical behavior, the pouch cells are simplified for modeling purposes. Each cell is represented by a 0.1 mm thick aluminum foil shell, which simulates the outer casing, and an 8 mm thick polymer gel core, serving as a surrogate for the internal active components, including the anode, cathode, and electrolyte. The pouch cells were represented using a homogenized model. This approach models the complex multi-layered jelly roll, that is composed of the anode, cathode and separator components, as a single, homogenous, and gel-like material. The material properties are determined to represent the quasi-fluid-like behavior of the jelly roll under impact, which is a common practice in vehicle-level crash simulations due to the high computational cost of modeling each individual layer. The simplified model effectively captures the cell core's mechanical response and energy absorption during impact, which is the most critical parameter for evaluating the structural integrity of the entire battery system. Validation of similar homogenized battery models has been documented in the literature [17,40–44]. However, this approach has limitations, as it does not capture the micro-scale phenomena that lead to internal short circuits and thermal runaway, or analyze local damage and show detailed stress and strain distributions of the individual components, limiting this study only to the macro-mechanical response of the battery pack, neglecting the electrochemical performance of the cells, as well as strain-rate-dependent phenomena.

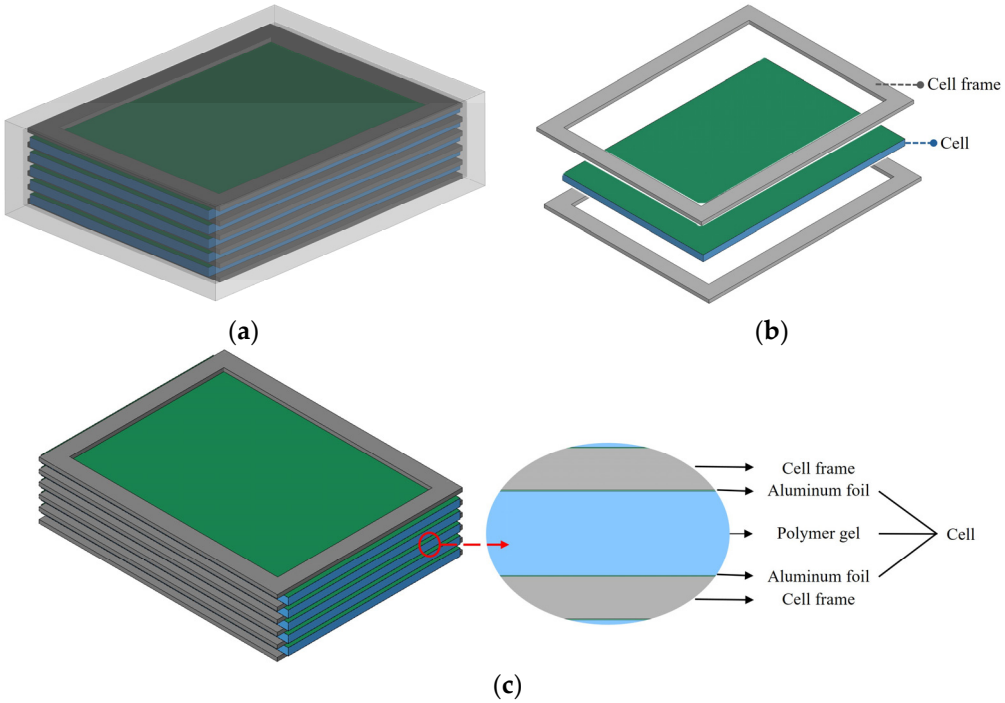

Figure 11. Geometry of (**a**) the cell pack, (**b**) the cell frames, and (**c**) the cells.

To limit uncontrolled motion of the cells during impact scenarios, plastic cell frames are introduced between each pouch cell. These frames have an orthogonal geometry of 270 mm × 210 mm, with a 4 mm thickness, and feature a central 236 mm × 175 mm opening to permit controlled deformation of the cells in the middle of the configuration, as shown in Figure 11b,c. For the finite element model, a mapped mesh was applied across all components to ensure mesh regularity and accuracy. The cell pack structure is discretized using 3 mm solid elements, while both the pouch cells and intermediate frames are meshed with a finer 2 mm element size, as depicted in Figure 12.

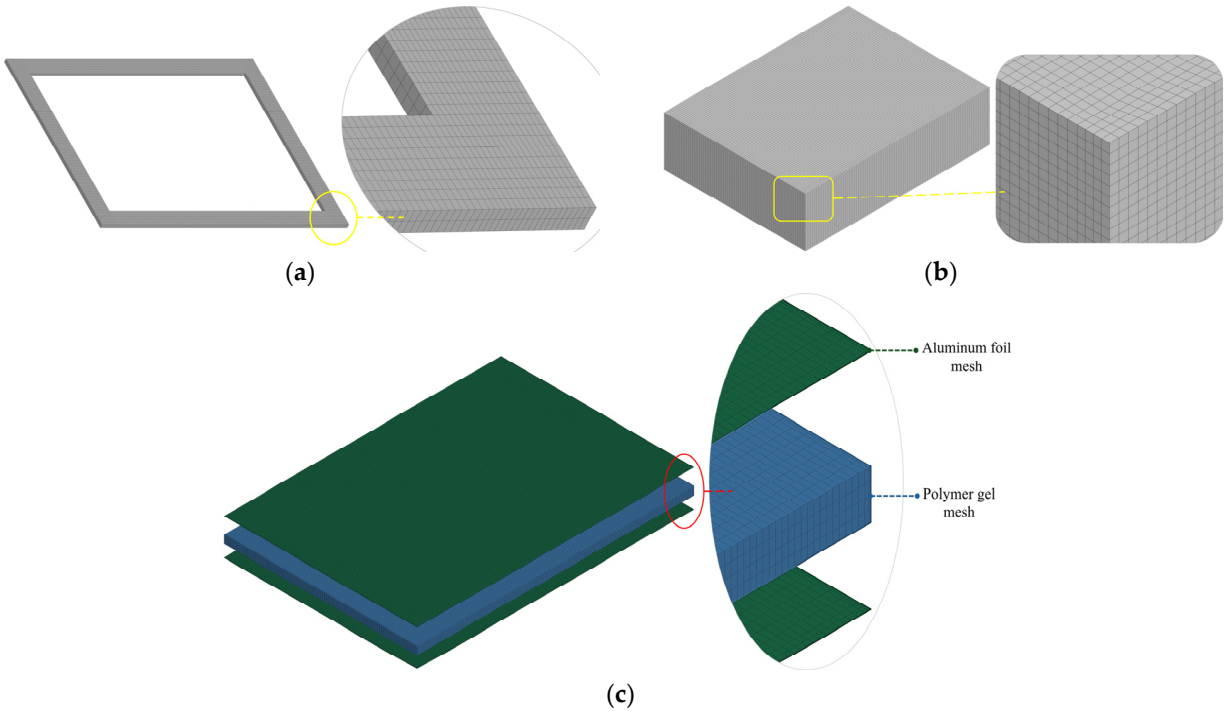

Figure 12. FE mesh of (**a**) the cell frame, (**b**) the cell pack, and (**c**) the cell.

Both the cell pack and the intermediate frames are composed of ABS plastic, a material commonly used for structural and protective components in battery systems. In the finite element model, ABS is represented using the MAT_24 (MAT_ISOTROPIC_ELASTIC_PLASTIC) material model in LS-DYNA, which accounts for isotropic plasticity without built-in failure or erosion capabilities. This model is selected for its computational efficiency and ability to capture basic plastic deformation behavior under impact loading. To enable failure within this framework, the ADD_EROSION option is activated. This enhancement allows for element deletion when a predefined failure criterion is met. In this study, the Von Mises stress criterion is employed, and failure is initiated when the equivalent stress reaches a specified threshold, as detailed in Table 7. For the cell components, an isotropic elastic material, with the specialization of allowing the modeling of fluids (MAT_ELASTIC), is employed. The input parameters for the aluminum foil and the polymer gel are stated in Table 8.

Table 7. Material input data for ABS properties.

Parameter	Value
	MAT_12
Density, RO	1040 kg/m^3
Shear modulus, G	0.85 GPa
Yield stress, SIGY	41.5 MPa
Bulk modulus, BULK	3.94 GPa
	MAT_ADD_EROSION
Equivalent stress at failure, SIGVM	55 MPa

Table 8. Material parameters of the cell components implemented in MAT_01.

Parameter	Value	
	Aluminum foil	**Polymer gel**
Density, RO	2700 kg/m^3	900 kg/m^3
Young's modulus, E	69 GPa	1.5 GPa
Poisson's ratio, PR	0.33 (-)	0.45 (-)

To accurately capture the mechanical interactions within the battery system, automatic surface-to-surface contact is defined between the cell pack and both the upper and lower support frames, as well as between the frames and individual pouch cells. This contact setup allows for realistic relative motion and stress transfer between components during impact loading. The internal cell structure, comprising the aluminum foil shell and the polymer gel core, is modeled using CONTACT_TIED_SURFACE_TO_SURFACE. In this constraint-based formulation, the slave nodes (assigned to the foil shell) remain fully attached to the master surface (the gel core), ensuring kinematic compatibility and preventing artificial separation or delamination during deformation. Additionally, the entire cell pack is assumed to be adhesively bonded to the composite housing via a tiebreak contact formulation. This is implemented using CONTACT_AUTOMATIC_SURFACE_TO_SURFACE_TIEBREAK, allowing for the simulation of interface failure between the cell pack and the housing. The relevant interfacial strength and failure criteria are described in Section 3.2, enabling the model to realistically predict debonding or delamination under severe loading conditions.

3.3. Crash (Pole) Model

Crash simulations, especially those involving pole impacts, represent some of the most demanding and safety-critical load cases for battery enclosures. These scenarios are

vital for evaluating the enclosure's ability to withstand localized, high-energy impacts, namely conditions commonly encountered in real-world vehicle collisions. Such analyses are crucial for assessing the enclosure's performance in terms of impact energy absorption, structural integrity preservation, and protection of the internal cell pack, while also considering material efficiency and weight optimization. In this study, a parametric analysis is performed to examine the impact response of the SMC composite battery housing across a range of impact energy levels. The simulations involve a cylindrical pole impactor striking the enclosure at various initial velocities, carefully selected to replicate realistic crash conditions observed in full-scale vehicle tests. These velocities, detailed in Table 9, correspond to practical, high-risk scenarios and offer valuable insights into the crashworthiness and structural resilience of the composite housing design.

Table 9. Pole impact model parameters.

	Impactor's Initial Velocity	Total Energy
i.	10 m/s	350 J
ii.	12.5 m/s	547 J
iii.	15 m/s	787 J

The crash simulation model consists of the main enclosure (housing) and lid, which are adhesively bonded, a rigid cylindrical impactor, and a base plate that simulates the vehicle floor, as depicted in Figure 13. The housing is made from SMC composite material, while both the impactor and base plate are modeled with steel properties. The impactor is modeled as a rigid body, measuring 120 mm in length, 50 mm in diameter, and weighing 7 kg. It is constrained to move exclusively in the x-direction, replicating a lateral impact scenario. The base plate, with dimensions of 440 mm × 300 mm, is also defined as a rigid body, with all translational and rotational degrees of freedom fully constrained. All components are meshed with solid elements using a uniform element size of 2 mm, ensuring sufficient resolution for capturing local deformations. Contact between the impactor and the housing/lid assembly is defined using CONTACT_AUTOMATIC_SURFACE_TO_SURFACE, allowing accurate simulation of force transmission during the impact event. To represent the adhesive bonding between the lid and housing, a tiebreak contact formulation is used, enabling simulation of potential debonding or failure under high loads. Additionally, the bottom surface of the housing is bonded to the base plate using adhesive film properties consistent with those defined in Table 5, ensuring realistic interface behavior during impact loading.

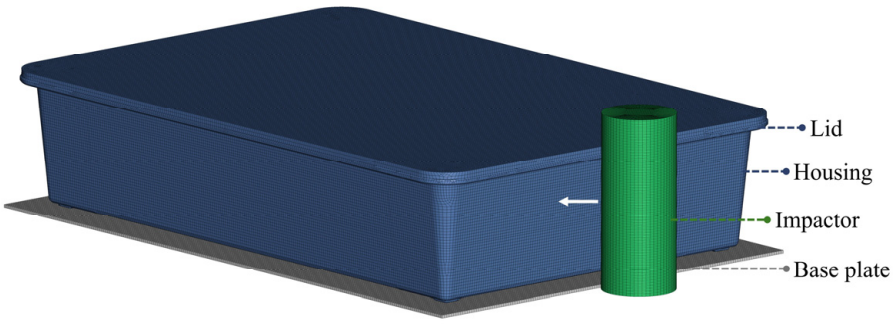

Figure 13. FE mesh of the housing and the impactor of the pole impact/crash model.

3.4. Discussion of Model Limitations

Although the proposed simulation framework is established to reproduce the global crashworthiness of the thermoplastic SMC battery housing, several limitations have to be

acknowledged. The first concerns material anisotropy. The MAT_162 model, while effective in capturing overall stiffness degradation, energy absorption, and force–displacement behavior, simplifies the heterogeneous nature of the SMC composite. By treating the material as a transversely isotropic laminate, the model neglects the complex microstructure of randomly oriented short fibers. As a result, it cannot explicitly capture the microscale failure mechanisms such as fiber pull-out, fiber–matrix debonding, delamination, or irregular crack propagation. This can lead to damage morphologies that are smoother and more idealized in the simulations than the experimentally observed.

A second limitation relates to strain-rate dependence. In this work, rate sensitivity was included in MAT_162 through the activation of strain-rate hardening parameters. While this ensures that the simulations incorporate the stiffening effect of dynamic loading, the parameters were based on literature data rather than direct experimental calibration of the Elium-based SMC composite. This approach provides a reasonable approximation of dynamic response but introduces uncertainty in representing the exact behavior of the material under varying strain rates and loading conditions.

The simplification of the battery cell model is another important limitation. Each pouch cell was represented by an aluminum shell encapsulating a homogenized polymer gel core, which captures the bulk deformation response while enabling computational efficiency. However, this approach cannot reproduce electrochemical failure mechanisms, and neglects strain-rate phenomena, which are an inherited characteristic of the cell component materials. In the same context, the present work is purely mechanical and does not incorporate multi-physics coupling, both electrochemical, mechanical and thermal. In batteries these interactions can strongly influence safety outcomes. These coupled phenomena were beyond the scope of this study but should be considered in future work to provide a more comprehensive view for battery safety.

Despite these limitations, the model remains a valuable tool for assessing structural-level crashworthiness, global energy absorption, and load transfer in thermoplastic battery enclosures. Future work will incorporate high-strain-rate experimental characterization, multi-scale material modeling, more detailed pouch cell representations, and coupled analyses to enhance predictive capability.

4. Numerical Results and Discussion

4.1. Model Validation Against Experimental Results

This section presents a detailed validation of the drop tower finite element models, through direct comparison with the experimental impact test results described in Section 2.3. Validation is a critical step to ensure the accuracy and predictive capability of the simulations, particularly in assessing the impact performance of the battery enclosure under realistic conditions. The comparison focuses on key impact response metrics, including force–time histories, damage patterns, and deformation and failure measurements, to evaluate how well the numerical predictions replicate the actual material and structural behavior under dynamic loading. By examining the level of agreement between simulation outputs and experimental observations, this validation effort aims to establish the models as credible and reliable tools for further parametric studies and design optimization.

4.1.1. Impact on SMC Plate: 7.5 J

The impact behavior of composite materials is typically evaluated using force–time curves, which provide insight into the dynamic response of the material during impact. In the 7.5 J impact case, illustrated in Figure 14, the experimental force–time response exhibits a smooth, symmetric, bell-shaped profile, characteristic of a non-perforating impact where the material undergoes deformation followed by rebound. The curve reaches a peak force of

0.486 kN at 7.55 ms, before returning to zero, marking the end of the impact event. The total impact duration is approximately 15 ms, and is consistent between the experimental and simulated results. The numerical force–time curve closely mirrors the experimental one in both shape and duration. The simulation predicts a peak force of approximately 0.512 kN, occurring slightly later, at around 7.91 ms, a difference well within acceptable tolerance limits for dynamic simulations. Both curves display a gradual rise to peak load, followed by a smooth unloading phase, indicating good correlation in the overall mechanical response. In the initial loading phase of the experimental curve (0–1 ms), the contact force increases with minor amplitude oscillations, likely due to elastic wave propagation and vibrations within the composite during early impact. This is followed by small load drops, which may correspond to localized stiffness reductions caused by the onset of damage, such as matrix cracking. These fluctuations are typical in experimental data and can be attributed to machine vibrations and external noise, which are inherently smoothed out in numerical simulations. The simulation curve is therefore smoother, as it does not capture these high-frequency disturbances. Nonetheless, the close agreement in peak force values, with the simulation differing by less than 5% from the experimental result, demonstrates strong predictive accuracy of the model for this energy level.

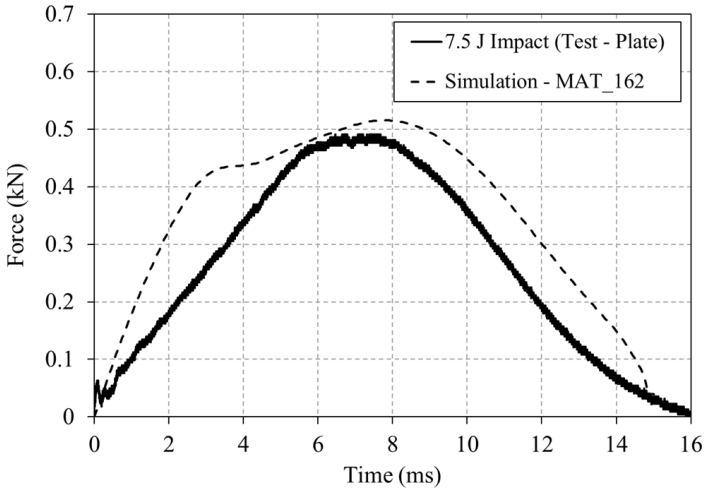

Figure 14. Experimental and numerical force–time curves for the 7.5 J impact of the drop tower impact on the plate.

At the impact energy of 7.5 J, the SMC composite material absorbs energy primarily through plastic deformation and localized damage mechanisms. The impact results in surface indentation, accompanied by matrix cracking and potentially minor fiber damage, without full penetration of the specimen by the impactor. As shown in Figure 15a, a comparison is made between the front face damage observed in the drop tower test and that predicted by the numerical simulation. The experimental specimen exhibits a distinct indentation with visible radial cracks resembling the projectile's shape, attributed to matrix failure. The measured damage dimensions are 10.40 mm × 10.02 mm. The simulation predicts a slightly larger dent, measuring 10.78 mm × 10.05 mm, consistent with the higher peak force observed in the numerical force–time response. Despite minor differences, the agreement between simulation and experiment is very good. Figure 15b presents the rear face of the impacted plate. The experimental specimen shows a well-defined indentation with cracks propagating outward from the center of impact. The measured dimensions are 18.67 mm × 21.82 mm. The simulation reproduces the overall shape of the indentation but displays a smoother deformation profile, without capturing the matrix cracking and fiber breakage seen in the test. The predicted damage area is 15.62 mm × 17.36 mm,

slightly smaller than the experimental values. This discrepancy is primarily attributed to the material modeling approach. The MAT_162 material model treats the chopped fiber composite as a transversely isotropic, unidirectional (UD)-like laminate, rather than a true discontinuous fiber composite, which can affect the accuracy of predicted damage modes. A side profile comparison in Figure 15c reveals that the maximum indentation depth in the experiment is 0.77 mm, whereas the simulation predicts 1.06 mm. Given the complexity of the material and the impact event, this level of agreement is considered acceptable, further supporting the validity of the simulation model.

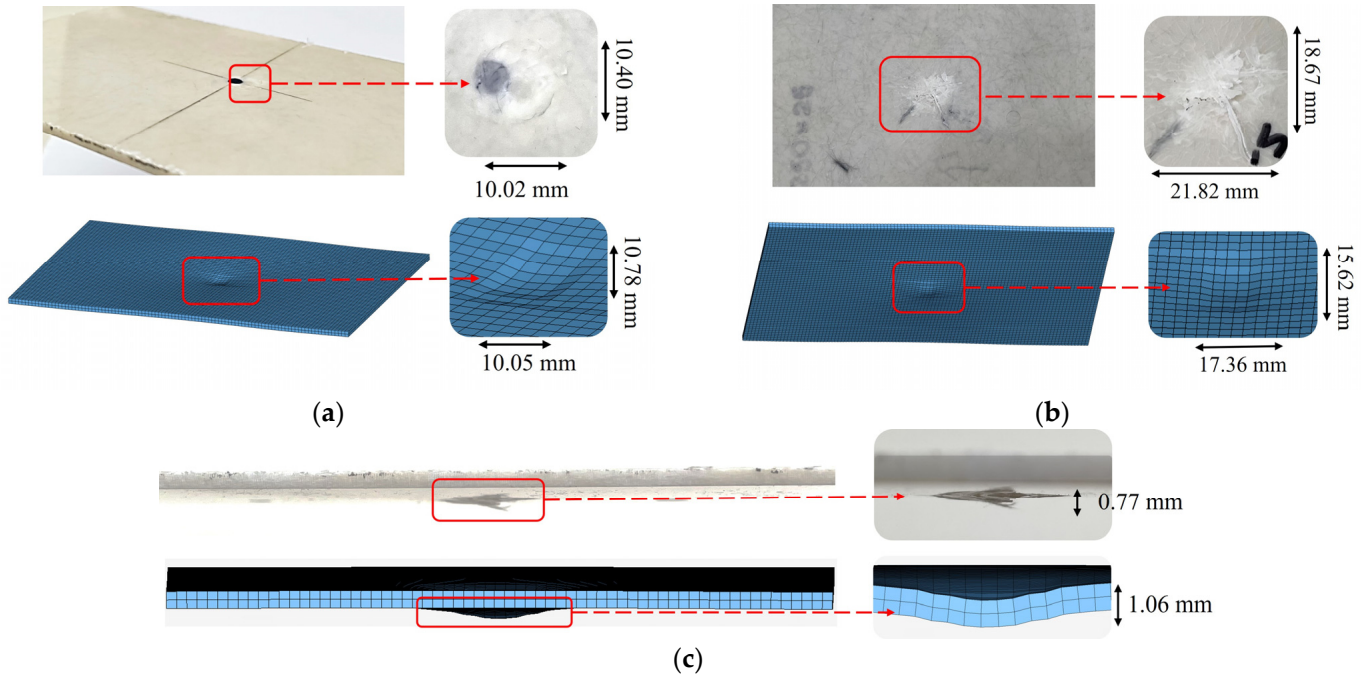

Figure 15. Experimental versus numerical results of the SMC plate subjected to 7.5 J impact. (**a**) Front face, (**b**) back face, (**c**) side profile comparison.

Overall, the results indicate that the MAT_162 material model effectively captures the stiffness and elastic–plastic behavior of the SMC composite throughout the impact event. The simulation accurately reproduces the general indentation morphology, though it lacks the fine resolution of crack propagation observed in the experimental specimens. Nevertheless, the depth of the damage is comparable between the simulation and experiment, suggesting that the model reliably captures the through-thickness deformation. While there are differences in the visual representation of damage, particularly in the depiction of matrix cracks, the close agreement in force–time response supports the model's validity in predicting energy absorption and macroscopic deformation behavior under low-energy impact conditions. This demonstrates the model's potential as a reliable tool for assessing the crashworthiness of composite battery enclosures at this energy level.

4.1.2. Impact on SMC Plate: 30 J

In the 30 J impact case, the experimental force–time curve, shown in Figure 16, displays a rapid initial rise, reaching a peak force of approximately 0.626 kN at 2.20 ms. Following this peak, the curve exhibits a complex profile, including a load drop indicative of fracture initiation, followed by a secondary peak of about 0.45 kN at 3.2 ms, and a subsequent sharp decline. This fluctuating behavior suggests a sequence of progressive failure mechanisms, such as matrix cracking and fiber breakage, occurring throughout the impact event. Additionally, part of this irregularity may be attributed to the experimental fixture

configuration, particularly the clamps. Under the high-energy impact, the clamps may have failed to maintain full constraint on the specimen, allowing minor relative movements that introduced oscillations into the measured force response. The total impact duration in the experiment is approximately 4.5 ms. The numerical simulation effectively captures the initial force rise and closely matches the primary peak, reaching approximately 0.643 kN at 2.4 ms, resulting in a 2.6% deviation from the experimental value. However, the simulation shows a shorter impact duration of about 4.1 ms and a smoother, more idealized decline in force after the peak. Notably, it does not reproduce the secondary peak, or the oscillatory features observed in the experimental data. This discrepancy is likely due to modeling simplifications and assumptions, such as idealized boundary conditions, rigid clamp definitions, and limitations in capturing dynamic interactions and complex damage progression, all of which contribute to the differences between simulated and observed behavior.

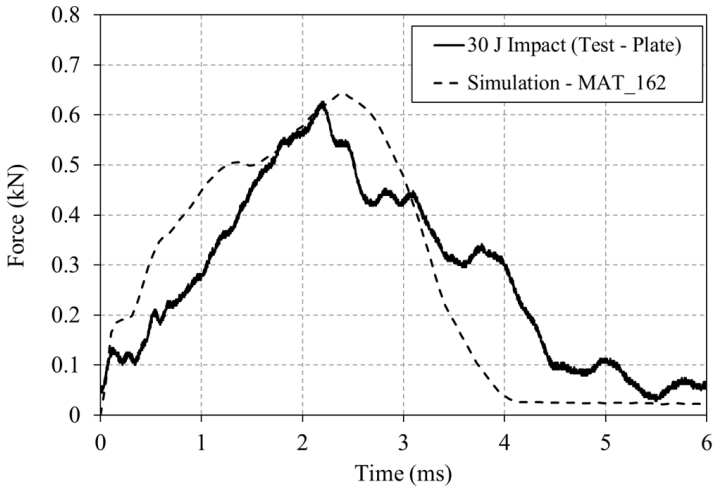

Figure 16. Experimental and numerical force–time curves for the 30 J impact of the drop tower impact on the plate.

A comparison between the experimental and numerical damage patterns reveals that the impactor fully penetrates the specimen in both cases, with the numerical model predicting a slightly larger perforation. This observation is consistent with the higher peak force observed in every simulation. As shown in Figure 17a, the front face of the specimen exhibits a clean, circular damage area in both the experimental and simulated results, corresponding closely to the geometry of the impactor. The damage dimensions are 13.27 mm × 13.27 mm in the experiment and 13.42 mm × 14.19 mm in the simulation, indicating strong agreement in damage extent on the impacted surface. On the rear face of the specimen (Figure 17b), the experimental test shows significant perforation, characterized by extensive matrix cracking, possible fiber breakage, and noticeable fiber pull-out around the hole's perimeter This results in an irregular damage shape with dimensions of approximately 18.29 mm × 17.37 mm. The numerical model, while unable to capture the detailed fiber fraying and pull-out due to limitations in the material formulation, predicts a smooth, circular perforation with dimensions of 18.50 mm × 18.41 mm, in very good agreement with the overall size of the damaged area. Figure 17c presents the side profile of the impact zone. The experimental specimen exhibits a penetration depth of 9.19 mm with visible signs of fiber separation. The simulation replicates the overall deformation shape, producing a slightly deeper penetration depth of 9.61 mm. Although the numerical result presents a more idealized failure profile, it successfully captures the macroscopic deformation behavior, even if it does not reflect the complex fiber damage mechanisms observed in the experiment.

The agreement between the experimental and numerical results is very good, particularly in terms of damage size and overall geometry. The simulation accurately predicts the macroscopic dimensions of the damage, including both the perforation diameter and the through-thickness deformation, indicating a high level of accuracy in capturing the global failure response of the SMC composite under impact. This serves as a critical validation point, reinforcing the model's capability to predict the overall extent of material failure in crash scenarios. However, notable differences in damage morphology are observed. These discrepancies, such as the absence of detailed fiber breakage and matrix cracking in the simulation, are inherent to continuum damage models like MAT_162. Such models are limited in their ability to represent micro-scale failure mechanisms, including fiber pull-out, delamination, and localized crack propagation, which are often visible in experimental observations. Despite these limitations, the model remains highly effective for predicting global damage metrics essential for structural design and crashworthiness assessment.

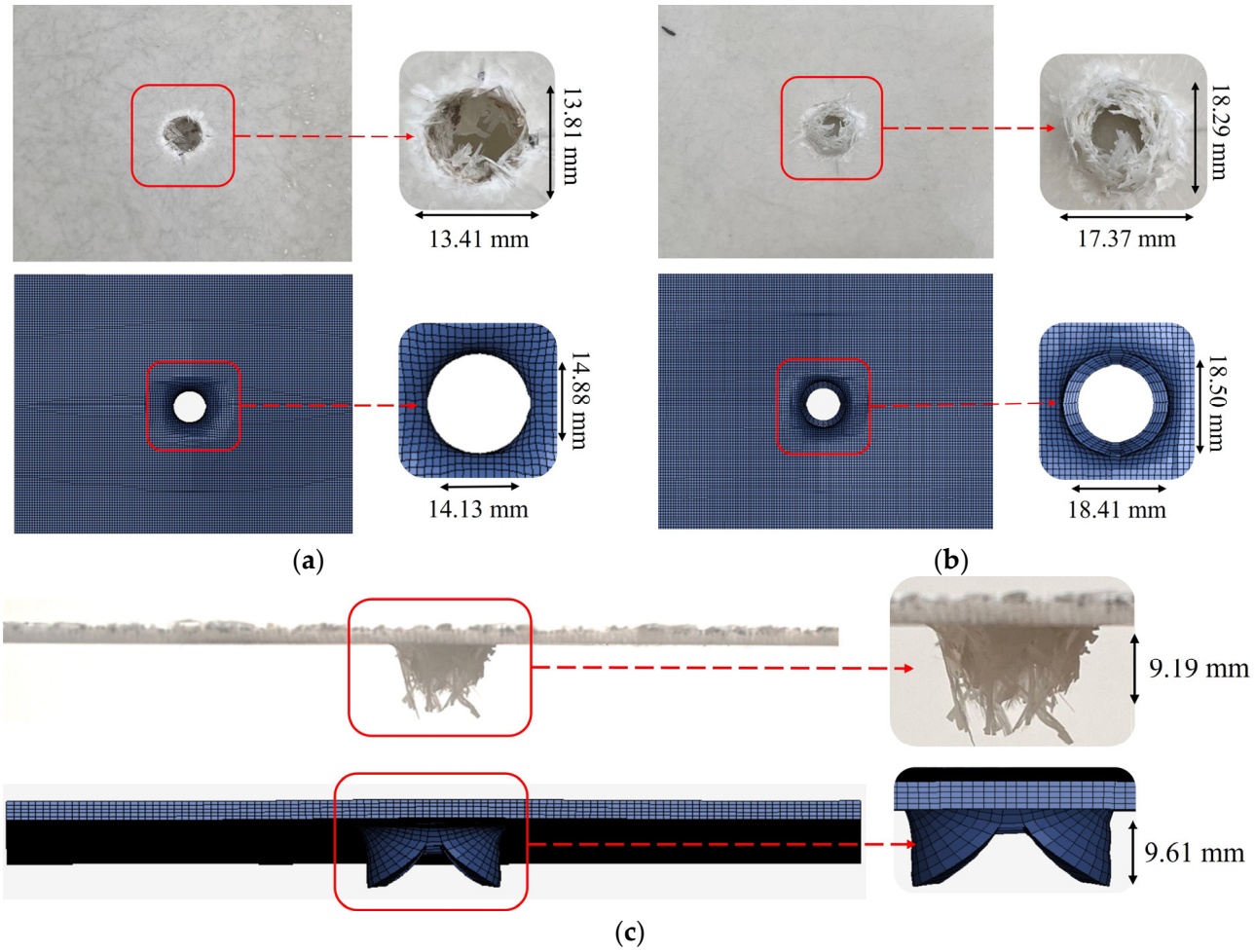

Figure 17. Experimental versus numerical results of the SMC plate subjected to 30 J impact. (**a**) Front face, (**b**) back face, (**c**) side profile comparison.

4.1.3. Impact on SMC Housing: 30 J

The overall profiles of the experimental and numerical force–time curves for the 30 J impact on the SMC housing, shown in Figure 18, demonstrate reasonably good agreement. Both curves exhibit a rapid initial force rise, reaching peak values of 0.737 kN (simulation) and 0.708 kN (experiment) at approximately 4.00 ms and 4.19 ms, respectively. This corresponds to a variation of just 3.9%, indicating a strong correlation in capturing the initial impact response. As with the 30 J plate impact case, the most notable differences

arise in the post-peak behavior. The experimental curve shows a sharp drop in force after approximately 5 ms, even dipping into negative values, which typically signals a major structural failure. This behavior is associated with degradation of local stiffness due to severe internal damage, such as matrix cracking, fiber breakage, and possible loss of constraint, ultimately signifying the fracture of the housing. In contrast, the simulation presents a more gradual decline in force, lacking the abrupt drop and negative force rebound observed in the experimental data. This discrepancy can be attributed to limitations in the material model, which may not fully capture the complex and dynamic failure mechanisms observed in the physical test, such as catastrophic fracture, debonding, or fixture compliance.

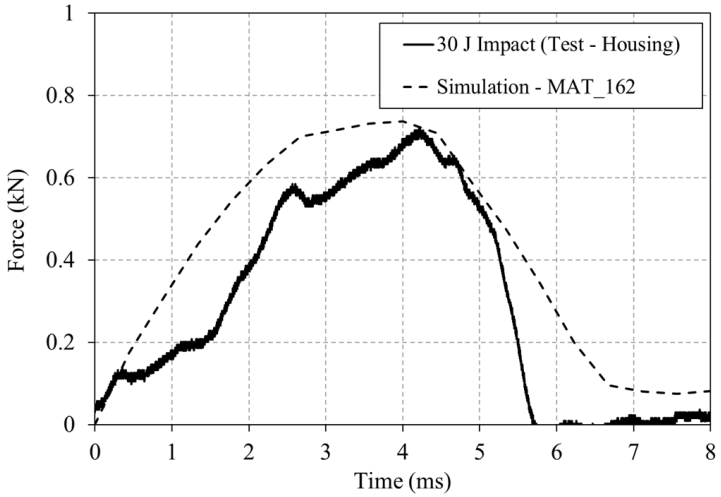

Figure 18. Experimental and numerical force–time curves for the 7.5 J impact of the drop tower impact on the housing.

The resulting damage on the housing surface under 30 J impact energy is comparable to that observed on the SMC plate tested at the same energy level, both in terms of damage dimensions and failure modes, as expected. On the front face of the housing, shown in Figure 19a, the experimental results reveal a symmetrical, circular opening caused by projectile penetration, with visible material damage measuring 13.27 mm × 13.27 mm. The simulation produces a similarly shaped, slightly cleaner perforation, with dimensions of 13.42 mm × 14.19 mm, demonstrating excellent agreement with the test. A consistent pattern is observed on the back face of the housing in Figure 19b, where the experimental damage exhibits a more irregular shape, attributed to fiber breakage and pull-out mechanisms. While the simulation cannot capture these finer-scale damage details due to material modeling limitations, it effectively reproduces the overall deformation profile. The side profiles of both the experiment and simulation, shown in Figure 19c, display significant plastic deformation, with measured indentation depths of 12.38 mm (experiment) and 12.17 mm (simulation). This close correlation in through-thickness deformation further validates the model's ability to predict global damage characteristics. Overall, the simulation shows very good agreement with experimental results in terms of damage size, shape, and deformation depth, thereby confirming the model's validity. It reliably captures damage patterns and force responses across different structural configurations, both plates and housing, demonstrating its applicability for predictive analysis in composite impact scenarios.

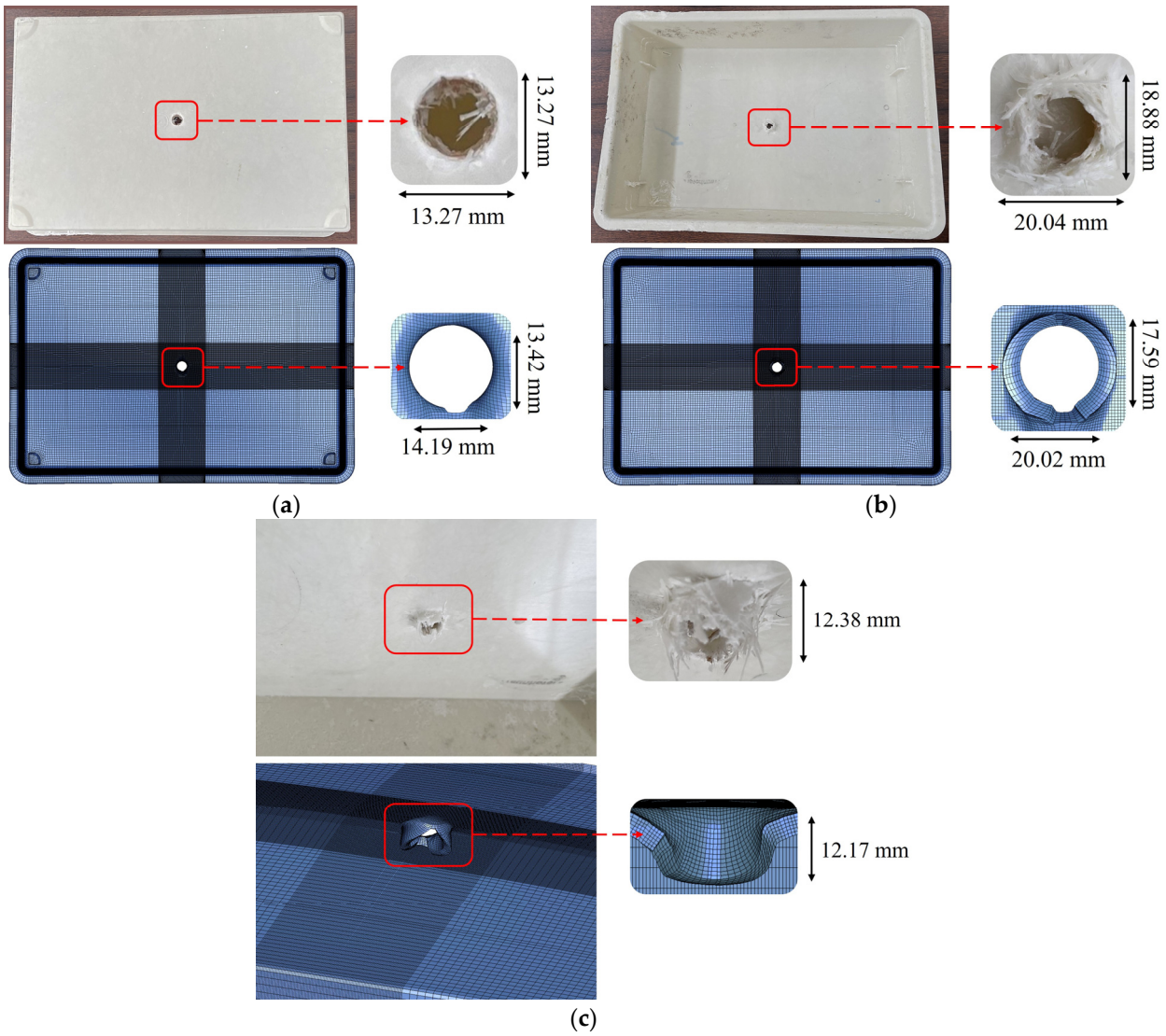

Figure 19. Experimental versus numerical results of SMC housing subjected to 30 J impact. (**a**) Front face, (**b**) back face, (**c**) side profile comparison.

4.2. Parametric Study on Impact Energy

4.2.1. Ground Impact

Figures 20 and 21 illustrate the progressive deformation and load transfer mechanisms in the parametric analysis of the battery housing's response to ground impact at increasing velocities. Figure 20 focuses on the maximum displacement of the housing and its interaction with the internal components of the cell pack, which closely aligns with the impactor's maximum displacement. At the lowest impact velocity (Figure 20a), the housing shows a maximum displacement of 4.74 mm, while the cell pack remains undisturbed, with a displacement of 3.71 mm. This results in a 1.28 mm residual gap between the cell pack and the first pouch cell. Individual cell displacement remains minimal (0.33–0.37 mm), indicating that the housing and cell pack effectively absorb impact energy, preventing direct loading on the cells. As velocity increases (Figure 20b), housing deformation rises to 6.86 mm, while the cell pack displaces 5.74 mm, reducing the gap to 0.65 mm. The first cell now exhibits a displacement of 1.10 mm, whereas the remaining four cells remain within 0.46–0.49 mm. While load transmission increases, there is still no direct impact loading on the cells. At 20 m/s (Figure 20c), the housing deformation reaches 7.78 mm and the cell pack displaces 6.71 mm, now making contact with the first cell, which shows localized

indentation of 2.71 mm. The remaining cells deform between 0.65 and 0.69 mm, indicating the onset of direct load transfer to the lowest cell in the stack. At the highest simulated velocity (Figure 20d), the housing's displacement increases to 11.20 mm, while the cell pack reaches 8.20 mm. The first cell is significantly deformed (4.17 mm) and the load propagates to the second cell, now showing 0.82 mm of displacement. The remaining three cells exhibit up to 0.79 mm of displacement, demonstrating load propagation through the cell stack. These results suggest that at impact velocities above 20 m/s, the housing's capacity to isolate the cell pack from high-energy impacts becomes compromised. This threshold is critical for defining design safety limits, as direct cell deformation increases the risk of mechanical failure and thermal runaway, posing significant safety concerns for battery systems in real-world crash scenarios.

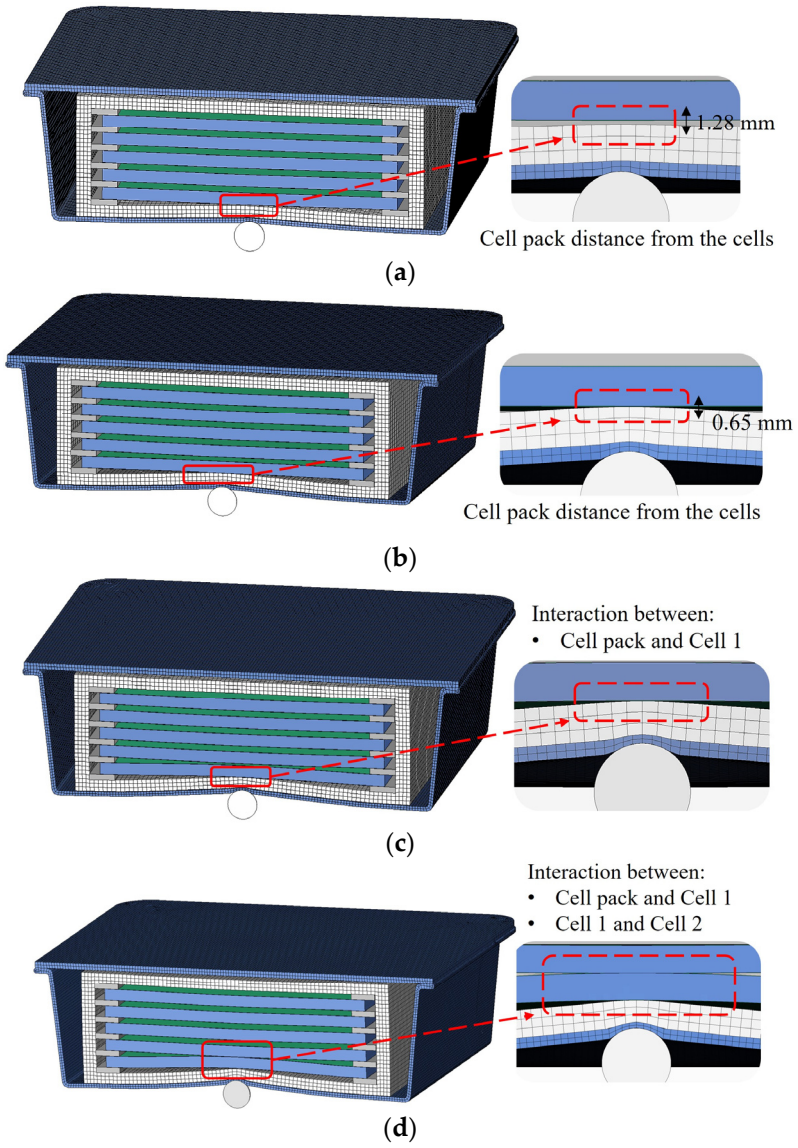

Figure 20. Interaction of the housing and the cells/cell pack at the maximum displacement of the impactor for the impact cases of (**a**) 10 m/s, (**b**) 15 m/s, (**c**) 20 m/s, and (**d**) 25 m/s.

Regarding the tiebreak contact behavior, the adhesive bonds between the cell pack and the housing, as well as between the housing and the lid, remain intact across all impact scenarios, indicating robust interfacial strength under dynamic loading. At an impact velocity of 10 m/s, the housing experiences a peak Von Mises stress of 114 MPa, localized around the impact area, while the majority of its surface remains within a lower stress range

of 30–40 MPa. The cell pack reaches a maximum stress of 38 MPa, while the cell frames and individual pouch cells experience peak stresses of 18 MPa and 8.5 MPa, respectively. These values confirm that mechanical loading at this velocity is well within safe operational limits, with no threat to the structural integrity of internal components. At 15 m/s, the stress distribution remains similar, with the housing peaking at 120 MPa, and the cell pack increasing marginally to 40 MPa. The stress in the cell frames and cells remains unchanged (18 MPa and 8.5 MPa, respectively), reaffirming that impact energy is still being effectively absorbed without compromising internal structures. At 20 m/s, a noticeable increase in stress levels occurs across all components. The housing reaches 156 MPa, while the cell pack, frames, and cells reach 41 MPa, 28 MPa, and 12.5 MPa, respectively. Although the housing approaches its damage threshold, all other components remain below critical stress limits, suggesting continued structural integrity. Under the highest impact velocity, the housing experiences 160 MPa, with the cell pack at 45 MPa, frames at 37 MPa, and cells at 16 MPa. At this level, localized damage in the housing is likely, but the internal components continue to operate within safe mechanical thresholds, showing no signs of failure. Overall, the stress analysis confirms that even under high-impact loading, the internal battery components remain mechanically protected, validating the efficacy of the housing design up to the maximum tested velocity.

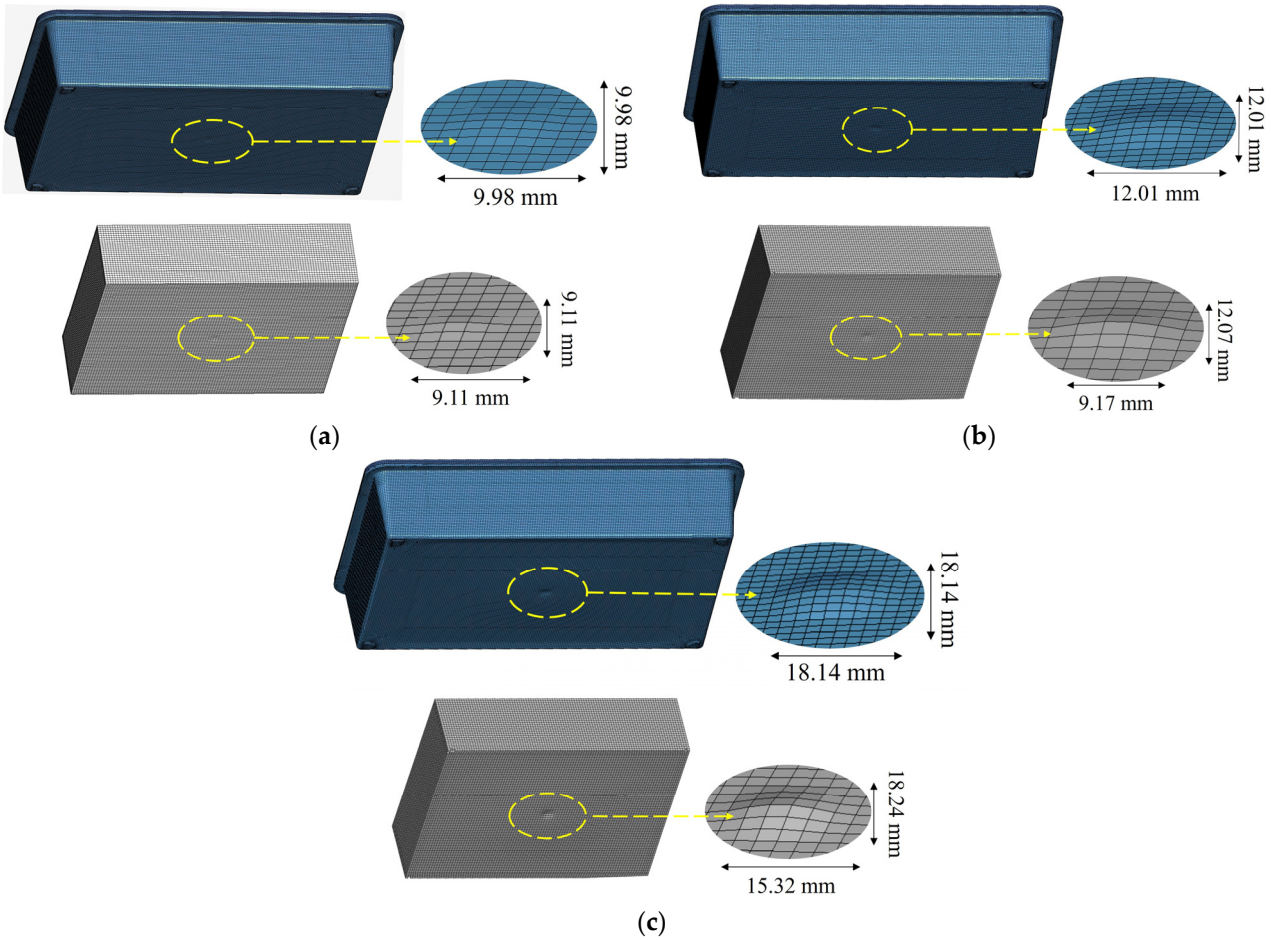

Figure 21. Permanent deformation in the x and y directions for the housing and the cell pack after being subjected to ground impact of (**a**) 15 m/s, (**b**) 20 m/s, (**c**) 25 m/s.

Regarding the permanent deformation of the housing and cell pack, the lowest impact velocity resulted in only minor indentation, insufficient to be captured accurately in post-processing in terms of x and y coordinates. Table 10 summarizes the residual deformation

along the z-axis for each parametric scenario. At impact velocities of 10 and 15 m/s, the residual deformation remains below 1 mm, indicating a resilient structural response at moderate energy levels. However, with further increase in velocity, the indentation depth nearly doubles, marking a threshold beyond which significant permanent deformation occurs, particularly noticeable above 20 m/s. In most cases, the cell pack exhibits greater permanent deformation than the housing. This trend is attributed to differences in material stiffness and the application of a coarser mesh in the modeling of the cell pack, which may reduce stiffness numerically and increase localized compliance. Figure 21a illustrates the dent profiles for both components at 15 m/s, showing spherical indentations consistent with the impactor geometry. The dent dimensions are comparable for both the housing and cell pack, ranging between 9 and 10 mm. At 20 m/s, Figure 21b shows a similarly symmetrical dent on the housing, while the cell pack exhibits a narrower width along the x-axis, indicating a more concentrated deformation. At the highest tested impact velocity, Figure 21c depicts more pronounced dents on both the housing and the cell pack. Despite the increased depth, the overall geometric characteristics of the deformations remain consistent with those observed at lower velocities, reflecting the repeatable nature of the response in this configuration.

Table 10. Permanent deformation of the housing and the cell pack in the z direction after ground impact of 10, 15, 20, 25 m/s.

Impact Velocity		Permanent Deformation	
		Housing	**Cell Pack**
i.	10 m/s	0.07 mm	0.01 mm
ii.	15 m/s	0.57 mm	0.72 mm
iii.	20 m/s	1.01 mm	1.25 mm
iv.	25 m/s	1.07 mm	1.32 mm

4.2.2. Crash (Pole Impact)

Regarding the numerical results of the pole impact analysis, Figure 22 presents the progressive evolution of damage in both the battery housing and the cell pack as impact velocity increases. At the lowest impact energy level, illustrated in Figure 22a, significant plastic deformation is observed on the left side of the housing, the impact site. The housing exhibits a maximum displacement of 54.10 mm in the impact direction. The lid undergoes inward and upward folding, indicating a localized buckling response and confirming permanent structural deformation. Despite this, the remainder of the housing retains its original shape, and the cell pack remains undeformed, maintaining its rectangular geometry. This demonstrates the housing's effectiveness in isolating and protecting the internal components under low-energy impact. At the intermediate velocity scenario (Figure 22b), the housing undergoes more pronounced deformation, localized primarily at the impact zone. The left wall buckles inward with a displacement of 76.61 mm, and the lid experiences additional bending. This reflects the housing's continued function as an energy-absorbing structure. However, the deformation now approaches the cell pack, which is displaced upwards by 33.60 mm in the z-direction. This vertical displacement raises concerns about the operational integrity of the pack, as the internal chemical components within the pouch cells could potentially mix, increasing the risk of short circuit. This case indicates the onset of a safety threshold, beyond which the housing can no longer fully isolate the cells from high-energy impact effects. At the highest impact velocity (Figure 22c), the housing experiences severe and widespread deformation. The left wall is crushed and bent inwards, reaching a displacement of 79 mm, while the lid undergoes extreme buckling and displacement, signifying a critical loss of structural integrity. The

cell pack also deforms substantially, especially on the left side, aligning with the intrusion zone of the housing. This implies that mechanical damage to individual cells has likely occurred, posing a risk of internal short-circuiting and potentially triggering thermal runaway. This scenario highlights the limit of the housing's energy absorption capacity; although it absorbs substantial energy through plastic deformation, it fails to prevent internal component compromise under extreme loading.

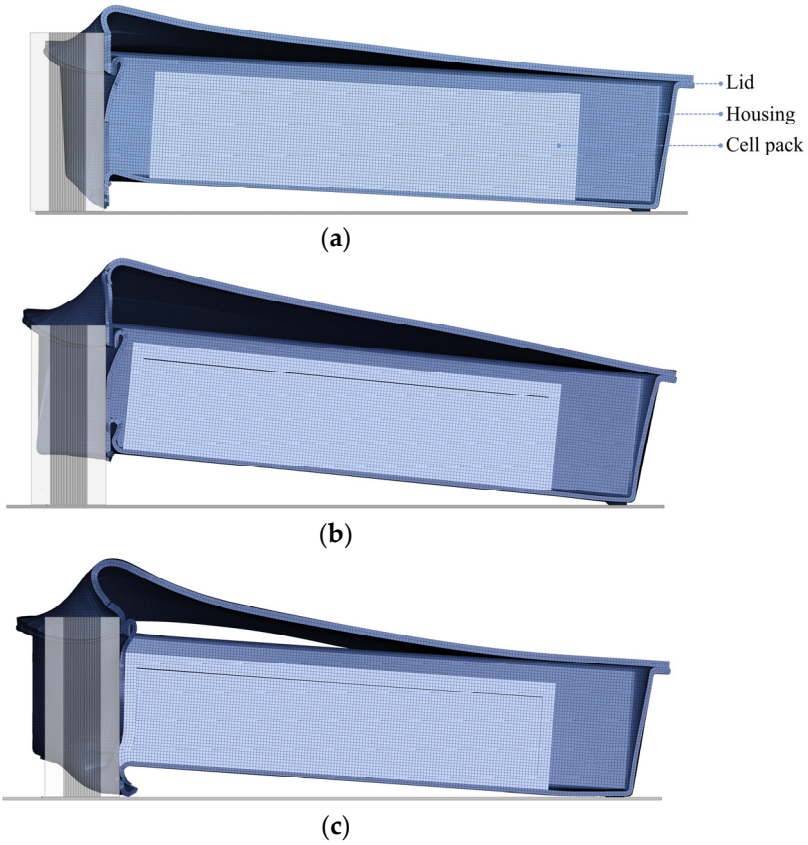

Figure 22. Maximum displacement of the housing and cell pack after the event of (**a**) 10 m/s, (**b**) 12.5 m/s and (**c**) 15 m/s pole impact.

Regarding tiebreak contact behavior, the bond between the left support legs and the base plate fails under loading, permitting the housing to displace in the z-direction. In the crash simulations at 10 and 12.5 m/s, the adhesive bond between the lid and the housing remains largely intact, aside from the immediate impact zone. Importantly, no debonding occurs between the cell pack and the housing in any of the three simulated impact cases. Figure 23 focuses on the most severe scenario: the 15 m/s pole impact. In this case, the housing undergoes substantial buckling and folding, fulfilling its role of energy absorption by sacrificing structural integrity to shield the internal components. However, the cell pack itself also experiences significant deformation, indicative of a high-energy impact, where progressive structural failure contributes to dissipating energy and preventing direct intrusion or catastrophic damage to the protected cells. Notably, the adhesive bond between the lid and the housing fails extensively, with a debonded length of 189.05 mm. While this separation allows the housing to deform more freely, enhancing energy absorption, it also alters the internal load paths and may influence the degree of cell pack protection. The debonding process is progressive, enabling relative movement between the lid and the housing, which contributes to the dissipation of impact energy, but could also reduce the enclosure's mechanical containment performance under extreme conditions.

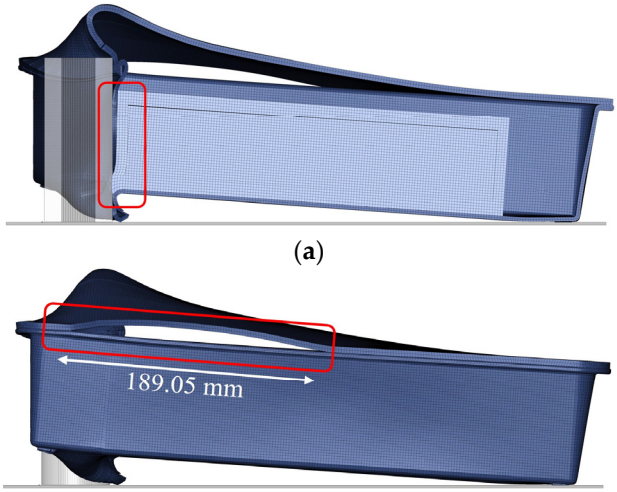

(**a**)

(**b**)

Figure 23. Interaction of the housing and the cell pack/lid at the maximum displacement of the impactor after the event of the 15 m/s pole impact: (**a**) left view (intersection), (**b**) right view.

5. Conclusions

This study investigates the impact performance of an innovative SMC-based thermoplastic battery housing under both ground and frontal pole impact scenarios. The mechanical behavior of the composite material was experimentally characterized through tensile, compressive, shear, and three-point bending tests. Drop tower impact experiments were conducted on flat SMC plates and the housing itself at 7.5 J and 30 J, providing the foundation for validating the corresponding finite element models.

Numerical simulations, developed using the LS-DYNA material model MAT_162, demonstrated strong correlation with experimental results, accurately predicting peak impact forces, global stiffness, and energy absorption. While the simulations offered smoother representations of localized failure phenomena, such as matrix cracking and fiber fracture, they still reliably captured key metrics including displacement, indentation depth, and overall damage extent.

Parametric analyses of ground impacts revealed a progressive failure mechanism: at low velocities, both the housing and cell pack provided effective isolation and protection for the battery cells. However, as velocity increased, the cell pack experienced greater displacement, leading to localized deformation in the first, and subsequently the second, cell layer—highlighting a critical velocity threshold beyond which internal damage becomes probable.

In frontal pole impact simulations, increasing impact energy resulted in pronounced deformation of the housing and lid. Although the enclosure initially dissipated energy effectively, its protective function diminished at higher energy levels, allowing mechanical intrusion into the cell pack. This observed degradation in performance under high-severity conditions provides valuable insights into the structural limits of the system.

From a safety standpoint, the structural integrity of the housing is correlated to battery safety, since deformation of the pouch cells may cause separator penetration and lead to internal short circuit that can potentially trigger thermal runaway. The parametric studies indicate that up to 15 m/s ground impact and 10 m/s pole impact, the Elium SMC housing successfully prevents contact between the impactor and the cell pack, ensuring that the cells remain mechanically isolated, maintaining their electrochemical safety. However, beyond these thresholds, the first pouch cells in the stack begin to deform. While the deformation observed in this study is not sufficient to cause immediate rupture, it highlights a critical transition point for defining safe operating conditions for battery housing design.

In summary, regarding the novelty of this work, it is the first study to investigate the impact response of a full-scale battery housing made from Elium-based sheet molding compound (SMC), integrating fire-retardant Martinal ATH. This work combines experimental testing, from mechanical characterization to drop-weight impacts, with validated LS-DYNA simulations, enabling accurate prediction of the housing's crashworthiness. This methodology can be deemed advanced for battery housings, since most prior studies either stop at coupon-level tests or focus only on numerical models. At the same time, through parametric ground and pole impact scenarios, the study identifies critical velocity thresholds beyond which pouch cell deformation initiates, providing safety design limits. Also, the housing is produced through SMC compression molding, showing feasibility for real-world EV applications, compared to laboratory-only studies. Overall, by linking structural crashworthiness with recyclability and fire safety, the study demonstrates the multifunctional potential of Elium-SMC composites for next-generation electric vehicle battery housings.

Author Contributions: A.F.: Data curation, Formal analysis, Investigation, Software, Validation, Writing—original draft. K.T.: Conceptualization, Funding acquisition, Methodology, Project administration, Resources, Supervision, Visualization, Writing—review and editing. All authors have read and agreed to the published version of the manuscript.

Funding: This work was financially supported by the EC-funded HORIZON Project "TEMPEST"-Project 101103681-. [HORIZON-CL5-2022-D2-01-05—Next generation technologies for High-performance and safe-by-design battery systems for transport and mobile applications (Batteries Partnership)].

Data Availability Statement: The original contributions presented in this study are included in the article. Further inquiries can be directed to the corresponding author.

Acknowledgments: All authors acknowledge support from Fraunhofer ICT, who provided the material samples and the CAD file of the housing to perform the mechanical tests and simulations.

Conflicts of Interest: The authors declare no conflicts of interest.

Abbreviations

The following abbreviations are used in the manuscript:

SMC	Sheet Molding Compound
BVID	Barely Visible Impact Damage
VID	Visible Impact Damage
BEV	Battery Electric Vehicle
VARI	Vacuum-Assisted Resin Infusion
RTM	Resin Transfer Molding
BPS	Battery Pack Systems/Structures
UD	Unidirectional
SOC	State of Charge
FEA	Finite Element Analysis
FML	Fiber Metal Laminate
BPE	Battery Pack Enclosure
ATH	Aluminum Hydroxide, $Al(OH)_3$
UTS	Ultimate Tensile Strength
GFRP	Glass Fiber-Reinforced Polymer
CZM	Cohesive Zone Modeling

References

1. Um, H.-J.; Hwang, Y.-T.; Bae, I.-J.; Kim, H.-S. Design and Manufacture of Thermoplastic Carbon Fiber/Polyethylene Terephthalate Composites Underbody Shield to Protect the Lithium-Ion Batteries for Electric Mobility from Ground Impact. *Compos. Part B Eng.* **2022**, *238*, 109892. [CrossRef]
2. Höhne, C.-C.; Blaess, P.; Ilinzeer, S.; Griesbaum, P. New Approach for Electric Vehicle Composite Battery Housings: Electromagnetic Shielding and Flame Retardancy of PUR/UP-Based Sheet Moulding Compound. *Compos. Part A Appl. Sci. Manuf.* **2023**, *167*, 107404. [CrossRef]
3. Kulkarni, S.S.; Hale, F.; Taufique, M.F.N.; Soulami, A.; Devanathan, R. Investigation of Crashworthiness of Carbon Fiber-Based Electric Vehicle Battery Enclosure Using Finite Element Analysis. *Appl. Compos. Mater.* **2023**, *30*, 1689–1715. [CrossRef]
4. *Revolutionizing Aircraft Materials and Processes*; Pantelakis, S., Tserpes, K., Eds.; Springer International Publishing: Cham, Switzerland, 2020; ISBN 978-3-030-35345-2.
5. Toro, S.A.; González, C.; Fernández-Blázquez, J.P.; Ridruejo, A. Fabrication and Mechanical Properties of a High-Performance PEEK-PEI Hybrid Multilayered Thermoplastic Matrix Composite Reinforced with Carbon Fiber. *Compos. Part A Appl. Sci. Manuf.* **2024**, *185*, 108308. [CrossRef]
6. Kazemi, M.E.; Shanmugam, L.; Lu, D.; Wang, X.; Wang, B.; Yang, J. Mechanical Properties and Failure Modes of Hybrid Fiber Reinforced Polymer Composites with a Novel Liquid Thermoplastic Resin, Elium®. *Compos. Part A Appl. Sci. Manuf.* **2019**, *125*, 105523. [CrossRef]
7. Kazemi, M.E.; Shanmugam, L.; Chen, S.; Yang, L.; Yang, J. Novel Thermoplastic Fiber Metal Laminates Manufactured with an Innovative Acrylic Resin at Room Temperature. *Compos. Part A Appl. Sci. Manuf.* **2020**, *138*, 106043. [CrossRef]
8. Sun, Q.; Liu, H.; Wang, Z.; Meng, Y.; Xu, C.; Wen, Y.; Wu, Q. Investigation on Thermal Runaway Hazards of Cylindrical and Pouch Lithium-Ion Batteries under Low Pressure of Cruise Altitude for Civil Aircraft. *Batteries* **2024**, *10*, 298. [CrossRef]
9. Höschele, P.; Ellersdorfer, C. Implementing Reversible Swelling into the Numerical Model of a Lithium-Ion Pouch Cell for Short Circuit Prediction. *Batteries* **2023**, *9*, 417. [CrossRef]
10. Shaikh, S.A.; Taufique, M.F.N.; Balusu, K.; Kulkarni, S.S.; Hale, F.; Oleson, J.; Devanathan, R.; Soulami, A. Finite Element Analysis and Machine Learning Guided Design of Carbon Fiber Organosheet-Based Battery Enclosures for Crashworthiness. *Appl. Compos. Mater.* **2024**, *31*, 1475–1493. [CrossRef]
11. Avdeev, I.; Gilaki, M. Structural Analysis and Experimental Characterization of Cylindrical Lithium-Ion Battery Cells Subject to Lateral Impact. *J. Power Sources* **2014**, *271*, 382–391. [CrossRef]
12. Pheysey, J.; Del Cuvillo, R.; Naya, F.; Pernas-Sanchez, J.; De Cola, F.; Martinez-Hergueta, F. Low-Velocity Impact Response of Hybrid Sheet Moulding Compound Composite Laminates. *Compos. Part A Appl. Sci. Manuf.* **2025**, *188*, 108527. [CrossRef]
13. Xu, D.; Pan, Y.; Zhang, X.; Dai, W.; Liu, B.; Shuai, Q. Data-Driven Modelling and Evaluation of a Battery-Pack System's Mechanical Safety against Bottom Cone Impact. *Energy* **2024**, *290*, 130145. [CrossRef]
14. Dai, Z.; Miao, Q.; Wu, D. Data Simulation of the Impact of Ball Strikes on the Bottom of Electric Vehicle Battery Packs Based on Finite Element Analysis. *Therm. Sci. Eng. Prog.* **2024**, *53*, 102757. [CrossRef]
15. Fragiadaki, A.; Tserpes, K. Numerical Simulation of Dynamic Response of a Composite Battery Housing for Transport Applications. *Eng. Proc.* **2025**, *90*, 10.
16. Li, R.; Pan, Y.; Zhang, X.; Dai, W.; Liu, B.; Li, J. Mechanical Safety Prediction of a Battery-Pack System under Low Speed Frontal Impact via Machine Learning. *Eng. Anal. Bound. Elem.* **2024**, *160*, 65–75. [CrossRef]
17. Chen, Y.; Santhanagopalan, S.; Babu, V.; Ding, Y. Dynamic Mechanical Behavior of Lithium-Ion Pouch Cells Subjected to High-Velocity Impact. *Compos. Struct.* **2019**, *218*, 50–59. [CrossRef]
18. Yin, H.; Ma, S.; Li, H.; Wen, G.; Santhanagopalan, S.; Zhang, C. Modeling Strategy for Progressive Failure Prediction in Lithium-Ion Batteries under Mechanical Abuse. *eTransportation* **2021**, *7*, 100098. [CrossRef]
19. Xu, J.; Liu, B.; Wang, X.; Hu, D. Computational Model of 18650 Lithium-Ion Battery with Coupled Strain Rate and SOC Dependencies. *Appl. Energy* **2016**, *172*, 180–189. [CrossRef]
20. Wang, W.; Xu, X.; Sun, S.; Wang, Y.; Zhang, T. Design and Uncertainty-Based Multidisciplinary Optimization of a 3D Star-Shaped Negative Poisson's Ratio Structural Battery Pack. *Energy* **2024**, *313*, 133728. [CrossRef]
21. Xia, Y.; Wierzbicki, T.; Sahraei, E.; Zhang, X. Damage of Cells and Battery Packs Due to Ground Impact. *J. Power Sources* **2014**, *267*, 78–97. [CrossRef]
22. Akbari, E.; Voyiadjis, G.Z. Stress and Strain Characterization for Evaluating Mechanical Safety of Lithium-Ion Pouch Batteries under Static and Dynamic Loadings. *Batteries* **2024**, *10*, 309. [CrossRef]
23. Cardoso-Palomares, M.A.; Paredes-Rojas, J.C.; Flores-Campos, J.A.; Oropeza-Osornio, A.; Torres-SanMiguel, C.R. Impact Testing of Aging Li-Ion Batteries from Light Electric Vehicles (LEVs). *Batteries* **2025**, *11*, 263. [CrossRef]
24. Santosa, S.P.; Nirmala, T. Numerical and Experimental Validation of Fiber Metal Laminate Structure for Lithium-Ion Battery Protection Subjected to High-Velocity Impact Loading. *Compos. Struct.* **2024**, *332*, 117924. [CrossRef]

25. Scurtu, L.; Szabo, I.; Mariasiu, F.; Moldovanu, D.; Mihali, L.; Jurco, A. Numerical Analysis of the Influence of Mechanical Stress on the Battery Pack's Housing of an Electric Vehicle. *IOP Conf. Ser. Mater. Sci. Eng.* **2019**, *568*, 012054. [CrossRef]
26. Wang, S.; Guo, S.; Li, R.; Hu, Z.; Leng, Q. On Crashworthiness Design of Hybrid Metal–Composite Battery-Pack Enclosure Structure. *Mech. Adv. Mater. Struct.* **2025**, *32*, 2548–2559. [CrossRef]
27. Weber, F.; Dötschel, V.; Steinmann, P.; Pfaller, S.; Ries, M. Evaluating the Impact of Filler Size and Filler Content on the Stiffness, Strength, and Toughness of Polymer Nanocomposites Using Coarse-Grained Molecular Dynamics. *Eng. Fract. Mech.* **2024**, *307*, 110270. [CrossRef]
28. Guo, A.; Tao, X.; Kong, H.; Zhou, X.; Wang, H.; Li, J.; Li, F.; Hu, Y. Effects of Aluminum Hydroxide on Mechanical, Water Resistance, and Thermal Properties of Starch-Based Fiber-Reinforced Composites with Foam Structures. *J. Mater. Res. Technol.* **2023**, *23*, 1570–1583. [CrossRef]
29. Atiqah, A.; Ansari, M.N.M.; Kamal, M.S.S.; Jalar, A.; Afeefah, N.N.; Ismail, N. Effect of Alumina Trihydrate as Additive on the Mechanical Properties of Kenaf/Polyester Composite for Plastic Encapsulated Electronic Packaging Application. *J. Mater. Res. Technol.* **2020**, *9*, 12899–12906. [CrossRef]
30. Pheysey, J.; De Cola, F.; Martinez-Hergueta, F. Short Fibre/Unidirectional Hybrid Thermoplastic Composites: Experimental Characterisation and Digital Analysis. *Compos. Part A Appl. Sci. Manuf.* **2024**, *181*, 108121. [CrossRef]
31. LSTC. *LS-DYNA® Keyword User's Manual Volume I*; Livermore Software Technology Corporation: Livermore, CA, USA, 2018; p. 5298572243.
32. LSTC. *LS-DYNA® Keyword User's Manual Volume II Material Models*; Livermore Software Technology Corporation: Livermore, CA, USA, 2001; p. 158205945.
33. Cui, J.; Wang, S.; Wang, S.; Li, G.; Wang, P.; Liang, C. The Effects of Strain Rates on Mechanical Properties and Failure Behavior of Long Glass Fiber Reinforced Thermoplastic Composites. *Polymers* **2019**, *11*, 2019. [CrossRef]
34. Kothari, A.; Choi, H.; Zhao, H.; Joseph, P.; Li, G. Strain Rate Effects on Thermoplastic Composites with Mechanical Interlocking. *Polym. Compos.* **2021**, *42*, 6332–6348. [CrossRef]
35. Gama, B.A.; Gillespie, J.W. Finite Element Modeling of Impact, Damage Evolution and Penetration of Thick-Section Composites. *Int. J. Impact Eng.* **2011**, *38*, 181–197. [CrossRef]
36. Kara, A.; Tasdemirci, A.; Guden, M. Modeling Quasi-Static and High Strain Rate Deformation and Failure Behavior of a (±45) Symmetric E-Glass/Polyester Composite under Compressive Loading. *Mater. Des.* **2013**, *49*, 566–574. [CrossRef]
37. Deka, L.J.; Bartus, S.D.; Vaidya, U.K. Damage Evolution and Energy Absorption of E-Glass/Polypropylene Laminates Subjected to Ballistic Impact. *J. Mater. Sci.* **2008**, *43*, 4399–4410. [CrossRef]
38. Birleanu, C.; Pustan, M.; Cioaza, M.; Bere, P.; Contiu, G.; Dudescu, M.C.; Filip, D. Tribo-Mechanical Investigation of Glass Fiber Reinforced Polymer Composites under Dry Conditions. *Polymers* **2023**, *15*, 2733. [CrossRef] [PubMed]
39. Dogan, F.; Hadavinia, H.; Donchev, T.; Bhonge, P. Delamination of Impacted Composite Structures by Cohesive Zone Interface Elements and Tiebreak Contact. *Open Eng.* **2012**, *2*, 612–626. [CrossRef]
40. Pan, Z.; Li, W.; Xia, Y. Experiments and 3D Detailed Modeling for a Pouch Battery Cell under Impact Loading. *J. Energy Storage* **2020**, *27*, 101016. [CrossRef]
41. Zhu, J.; Wierzbicki, T.; Li, W. A Review of Safety-Focused Mechanical Modeling of Commercial Lithium-Ion Batteries. *J. Power Sources* **2018**, *378*, 153–168. [CrossRef]
42. Jeong, H.-Y.; Park, J. Development of a Homogenized Finite Element Model for Pouch Lithium-Ion Battery Cells Considering Porosity and Pressure Sensitivity. *Energies* **2024**, *17*, 1162. [CrossRef]
43. Beaumont, R.; Masters, I.; Das, A.; Lucas, S.; Thanikachalam, A.; Williams, D. Methodology for Developing a Macro Finite Element Model of Lithium-Ion Pouch Cells for Predicting Mechanical Behaviour under Multiple Loading Conditions. *Energies* **2021**, *14*, 1921. [CrossRef]
44. Wang, H.; Duan, X.; Liu, B. The Anisotropic Homogenized Model for Pouch Type Lithium-Ion Battery Under Various Abuse Loadings. *J. Electrochem. Energy Convers. Storage* **2021**, *18*, 021015. [CrossRef]

Disclaimer/Publisher's Note: The statements, opinions and data contained in all publications are solely those of the individual author(s) and contributor(s) and not of MDPI and/or the editor(s). MDPI and/or the editor(s) disclaim responsibility for any injury to people or property resulting from any ideas, methods, instructions or products referred to in the content.